

MIT Open Access Articles

*Gas Separations using Nanoporous Atomically Thin Membranes:
Recent Theoretical, Simulation, and Experimental Advances*

The MIT Faculty has made this article openly available. **Please share**
how this access benefits you. Your story matters.

Citation: Yuan, Zhe, He, Guangwei, Li, Sylvia Xin, Misra, Rahul Prasanna, Strano, Michael S et al. 2022. "Gas Separations using Nanoporous Atomically Thin Membranes: Recent Theoretical, Simulation, and Experimental Advances." *Advanced Materials*, 34 (32).

As Published: 10.1002/ADMA.202201472

Publisher: Wiley

Persistent URL: <https://hdl.handle.net/1721.1/145712>

Version: Final published version: final published article, as it appeared in a journal, conference proceedings, or other formally published context

Terms of use: Creative Commons Attribution NonCommercial License 4.0



Gas Separations using Nanoporous Atomically Thin Membranes: Recent Theoretical, Simulation, and Experimental Advances

Zhe Yuan, Guangwei He, Sylvia Xin Li, Rahul Prasanna Misra, Michael S. Strano,* and Daniel Blankschtein*

Porous graphene and other atomically thin 2D materials are regarded as highly promising membrane materials for high-performance gas separations due to their atomic thickness, large-scale synthesizability, excellent mechanical strength, and chemical stability. When these atomically thin materials contain a high areal density of gas-sieving nanoscale pores, they can exhibit both high gas permeances and high selectivities, which is beneficial for reducing the cost of gas-separation processes. Here, recent modeling and experimental advances in nanoporous atomically thin membranes for gas separations is discussed. The major challenges involved, including controlling pore size distributions, scaling up the membrane area, and matching theory with experimental results, are also highlighted. Finally, important future directions are proposed for real gas-separation applications of nanoporous atomically thin membranes.

1. Introduction

Separation processes account for nearly half of the energy consumption in the industrial sector and 10–15% of the world's total energy consumption.^[1–3] The enormous production scale of chemical commodities is an important reason for the high energy consumption. The dominance of thermal-based separation processes, including distillation and evaporation, is another reason.^[4] These thermal-based separations rely on phase changes and are highly energy intensive, accounting for more than 80% of the energy consumed by chemical separations.^[4] On the other hand, membrane separations, driven by pressure differences, are much more energy efficient and environmentally friendly because they do not require extensive heating or


cooling.^[1] However, much improvement is required for the membranes to be competitive application-wise.^[5,6]

The separation of gaseous mixtures is essential in the chemical industry, including hydrogen separation in ammonia or petrochemical plants, nitrogen separation from air, CO₂ separation in natural gas processing,^[7] olefin/paraffin separation,^[1] and H₂S separation from sour gas.^[8] Similar to separation processes in general, thermal-based gas-separation methods, such as cryogenic distillation, amine adsorption, and vapor condensation, consume a high amount of energy, which can be significantly reduced using gas-separation membrane units.^[5,8] A membrane that can separate

gases allows certain components in a mixture to permeate at higher rates than others. The economic competitiveness of a gas-separation membrane highly depends on its gas permeance K and its selectivity S . The permeance K_i of gas species i (in SI units of mol m⁻² s⁻¹ Pa⁻¹) is defined as $K_i = F_i/\Delta p_i$, where F_i (in SI units of mol m⁻² s⁻¹) is the flux of gas i through the membrane, and Δp_i is the partial pressure difference (the driving force) of gas i between the feed side and the permeate side. For relatively thick conventional membranes, whose cross-membrane transport resistance is dominated by the bulk interior, the permeance K_i is inversely proportional to the membrane thickness d . Correspondingly, the permeability P_i of gas i (in SI units of mol m⁻¹ s⁻¹ Pa⁻¹) is defined as $P_i = K_i d = F_i d/\Delta p_i$, which is an intrinsic property of a material. The selectivity S_{ij} between gases i and j is defined as $S_{ij} = K_i/K_j = P_i/P_j$.

Polymers have been the most widely used materials for gas-separation membranes for decades because of their relatively low cost and low manufacturing difficulty.^[8,9] However, membrane separations using state-of-the-art polymeric membranes cannot outcompete the thermal-based separation methods economically.^[7] One of the limitations of the polymeric membranes is the trade-off between permeability and selectivity, originally investigated by Robeson.^[10,11] The best combination of permeability and selectivity for a binary gas pair is referred to as the polymer upper bound. This trade-off originates from the interplay between the free volume spacing in the polymer matrices and the size of the gas molecules.^[12] Smaller polymeric spacing increases the selectivity but sacrifices the permeability due to the lower gas

Z. Yuan, G. He, S. X. Li, R. P. Misra, M. S. Strano, D. Blankschtein
 Department of Chemical Engineering
 Massachusetts Institute of Technology
 Cambridge, MA 02139, USA
 E-mail: strano@mit.edu; dblank@mit.edu

 The ORCID identification number(s) for the author(s) of this article can be found under <https://doi.org/10.1002/adma.202201472>.

© 2022 The Authors. Advanced Materials published by Wiley-VCH GmbH. This is an open access article under the terms of the Creative Commons Attribution-NonCommercial License, which permits use, distribution and reproduction in any medium, provided the original work is properly cited and is not used for commercial purposes.

DOI: 10.1002/adma.202201472

diffusivity inside the polymer, and vice versa. Note that this permeability-selectivity trade-off exist for all materials, but the upper bound for polymers can be surpassed by many other materials with more rigid pore structures, such as zeolites,^[13,14] metal organic frameworks (MOFs),^[15,16] silica,^[17] carbon-based materials,^[18–20] mixed matrix composites,^[21,22] and some polymers which are thermally rearranged.^[9] However, membranes made of the materials mentioned above are relatively thick (generally > 100 nm) due to the limitation of fabrication techniques and requirement for sufficient mechanical robustness. Furthermore, the permeability-selectivity trade-off constrains the permeability of a material in order to guarantee a reasonable selectivity. These two factors combined lead to low permeances through those conventional membrane materials ($K_i = P_i/d$).

Recent experimental and modeling advances in understanding the behavior of novel atomically thin 2D materials, including graphene,^[23–25] hexagonal boron nitride (hBN),^[26] and transition metal dichalcogenides (TMDs),^[27] offers great opportunities for potential breakthroughs in the membrane separation field.^[24,28] As mentioned above, gas permeance through a membrane is inversely correlated to its thickness.^[29] Therefore, porous atomically thin 2D materials show high promise as next-generation gas-separation membranes.^[28,30,31] Their high mechanical strength^[32] and chemical stability^[23,33] also enable them to serve as effective membranes. Note that defect-free atomically thin 2D materials are almost impermeable to any gases, except for an extremely low H₂ permeance through defect-free single-layer graphene.^[34–36] Therefore, pores need to be created in these 2D materials by removing a certain number of atoms. In order to discriminate between different gas molecules whose kinetic diameters are typically 0.2–0.6 nm, the diameter of these pores should be on the nanometer scale. The atomically thin membranes with nanometer-sized pores (or nanopores) are referred to as nanoporous atomically thin membranes (NATMs).^[30] Compared to pore matrices inside polymeric membranes, nanopores in NATMs have negligible pore lengths. As a result, gas transport through nanopores in NATMs experiences minimal internal resistance, and is instead dominated by the transport resistances at the pore entrance and at the pore exit. This important feature makes the solution-diffusion model not readily applicable to gas transport through NATMs.^[37]

Recently, significant progress has been made in using NATMs for gas separation, in terms of both theory and experiments. Nevertheless, much work is still needed to match theory with experimental measurements, as well as for the large-scale application of NATMs for gas separations. This review first summarizes recent theoretical and simulation advances in predicting gas permeances through nanopores in NATMs. Following that, recent experimental advances are reviewed, focusing on perforation strategies, pore size distributions, and supporting layers for NATMs. Subsequently, the review discusses the experimental validation of the theoretical predictions. Finally, the review discusses the future directions of NATMs. The outline of this review is highlighted in **Figure 1**. It is noteworthy that the review focuses on gas permeation through rigid nanopores in a continuous and atomically thin sheet, where the gas transport is governed by in-plane nanopores but not by interlayer channels or slits between nanosheets. For a discussion of gas permeation via interlayer diffusion or other transport mechanisms via other types of novel thin membranes, including 2D zeolites, 2D MOFs, laminar

graphene oxide, MXenes, or carbon nanomembranes, the reader is referred to the excellent reviews.^[24,38–43]

2. Theoretical and Simulation Advances

2.1. Analytical Descriptions

Gas transport through a nanopore in NATMs is governed by different mechanisms depending on the size of the nanopore (**Figure 2**). Nanopores in single-layer graphene are nearly circular,^[44] and their dimensions can be represented by their pore diameters D_p . Nanopores in hBN are typically triangular due to the different energy barriers associated with removing B or N atoms, but can also be hexagonal under an elevated synthesis temperature or upon using a high electron beam current for etching.^[45–49] Similarly, nanopores in TMDs such as MoS₂ can also be triangular or hexagonal, depending on the different perforation methods used.^[33,50,51] For simplicity, we will use the pore diameter D_p to represent the pore size in NATMs.

As shown in **Figure 2**, when the pore diameter D_p is larger than the gas mean free path λ (or equivalently, the Knudsen number $Kn = \lambda/D_p < 1$), the gas can be treated as a continuum fluid because a gas molecule can collide with other gas molecules while crossing the pore. The gas mean free path λ is the average distance travelled by a gas molecule between successive collisions, and is on the order of 100 nm at ambient pressure and room temperature.^[52] When $D_p > \lambda$, gas transport through the pore is dominated by collective gas flow, which can be predicted by the Navier–Stokes equations. An analytical solution to the Navier–Stokes equations exists when the membrane is modeled as an infinitesimally thin plate (which is a good approximation for NATMs), and is known as the modified Sampson's formula, given by^[53–55]

$$Q = \frac{D_p^3 \Delta p}{24 \mu_g} (1 - O(\kappa^{1.5})) \quad (1)$$

where Q is the volumetric flow rate through one pore, μ_g is the dynamic viscosity of the gas mixture, and κ is the membrane porosity. Because different gas components are well mixed and can exchange momenta when crossing the pore, the selectivity approaches 1 in this range.

When $D_p < \lambda \approx 100$ nm ($Kn > 1$), the cross-pore transport of a gas molecule is mostly not affected by other gas molecules and the continuum approximation breaks down. Specifically, gas transport is governed by effusion when $D_p \gg D_m$, where D_m is the gas kinetic diameter (typically 2–6 Å).^[56] Effusion, by definition, is the process where gas molecules escape through a pore without any interference from the other gas molecules (guaranteed by $D_p < \lambda$) or from the pore edge (guaranteed by $D_p \gg D_m$).^[57] Therefore, the rate of effusion is equal to the rate of impingement of the gas molecules onto the pore area from the bulk, and can be predicted by the kinetic theory of gases as follows^[58]

$$\frac{dn}{dt} = \frac{\Delta p A_p}{\sqrt{2\pi m k_B T}} = \frac{\Delta p}{\sqrt{2\pi m k_B T}} \cdot \frac{\pi D_p^2}{4} \quad (2)$$

where dn/dt is the molar gas permeation rate through the pore (mol s^{−1}), A_p is the pore area, m is the gas molecular weight, k_B

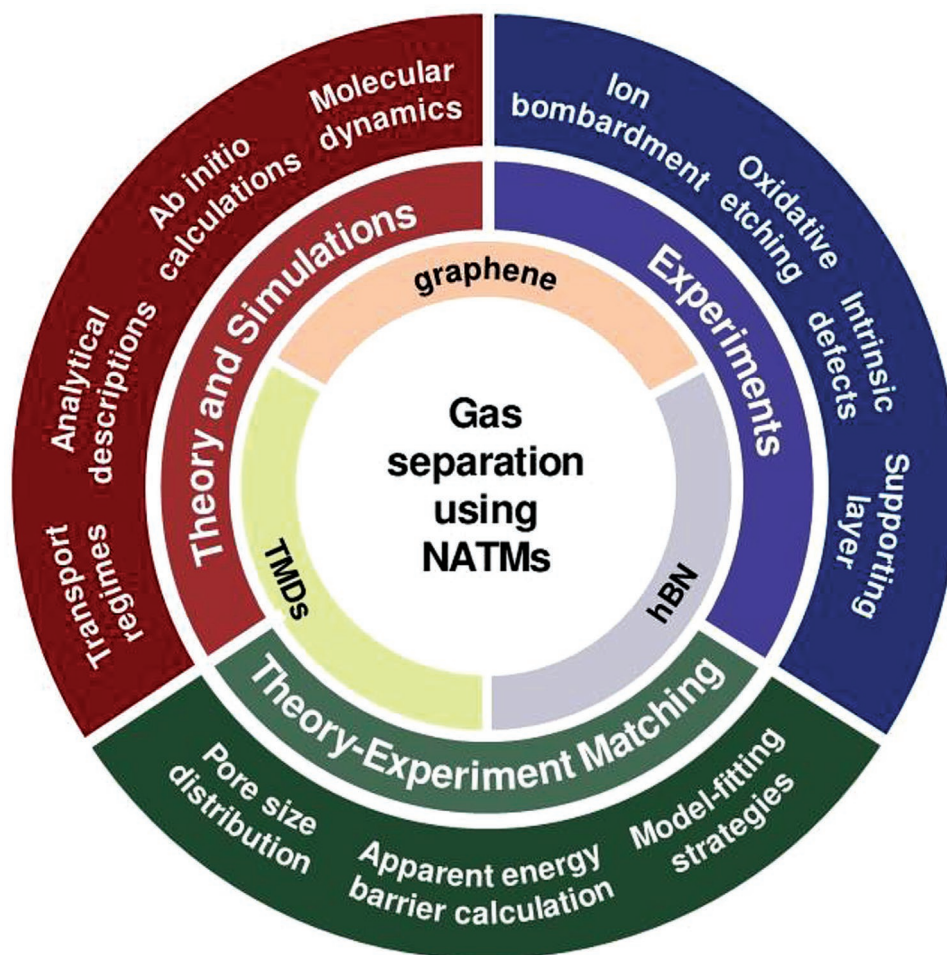


Figure 1. Overview and key concepts of this review on gas separation using nanoporous atomically thin membranes (NATMs).

is the Boltzmann constant, and T is the absolute temperature in degrees Kelvin. It is useful to define the permeance per pore Π (sometimes referred to in the literature as “permeance” in short),^[59,60] which is equal to the molar gas flow rate dn/dt normalized by the pressure difference Δp , that is

$$\Pi = \frac{1}{\Delta p} \cdot \frac{dn}{dt} \quad (3)$$

Note that the difference between Π (in $\text{mol s}^{-1} \text{Pa}^{-1}$) and permeance K (in $\text{mol m}^{-2} \text{s}^{-1} \text{Pa}^{-1}$) is that Π is not normalized by the total membrane area, and therefore, is more suitable to describe gas transport through individual pores in both theory and simulation studies. In contrast, permeance K is more often used in experimental studies. The two terms are connected by the areal pore density ρ : $K = \rho\Pi$. For gas permeation governed by effusion, the permeance per pore Π_{effusion} can be expressed as follows

$$\Pi_{\text{effusion}} = \frac{A_p}{\sqrt{2\pi m k_B T}} = \frac{1}{\sqrt{2\pi m k_B T}} \cdot \frac{\pi D_p^2}{4} \quad (4)$$

Correspondingly, the selectivity S_{12} between gas species 1 and 2 is given by

$$S_{12,\text{effusion}} = \sqrt{\frac{m_2}{m_1}} \quad (5)$$

which is known as Graham’s law of effusion, or the Knudsen selectivity.^[11]

Equation (4) is accurate in the limit when $D_p \gg D_m$, because the probability of gas permeation being affected by the pore edge is infinitesimally small. However, as D_p decreases and approaches D_m , the steric effect imposed by the pore edge becomes more pronounced and should be considered—not all the impingement attempts of gases become successful permeation events. In the range of $\lambda > D_p > 3D_m$, the pore is sufficiently large such that no energy barrier exists for gas permeation. In other words, an impingement attempt of a gas molecule will succeed if it avoids hitting the pore edge and getting bounced off. In this D_p range, gas permeation is still governed by effusion, but with a correction due to the steric effect.

A simplified correction to Equation (4) was proposed by Wang et al., where the pore area A_p is replaced by an effective pore area $A_{\text{eff}} \approx \pi(D_p - D_m)^2/4$.^[30] The idea is that only the central circle with diameter $D_p - D_m$ is accessible for gas impingements. Correspondingly, Π governed by effusion is corrected as follows (* denotes correction)

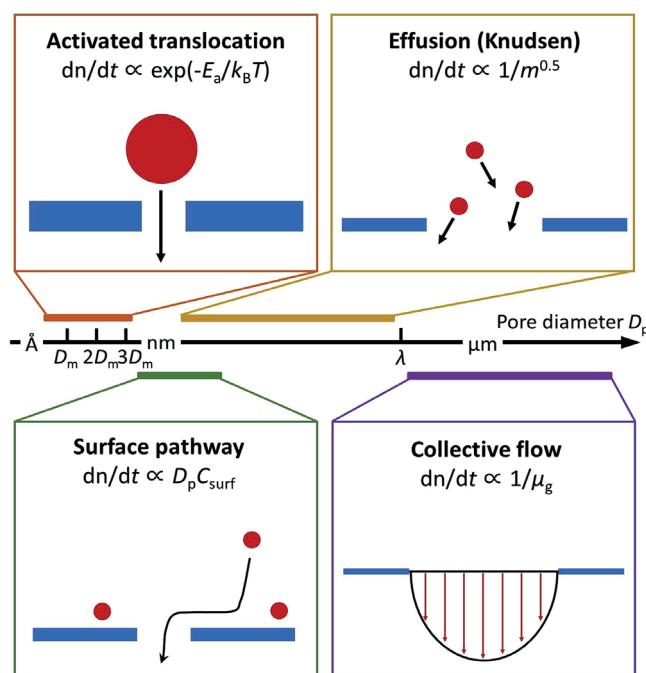


Figure 2. Schematic of gas transport mechanisms through nanopores in an NATM with different pore diameters. Red circle, gas molecule; blue sheet, NATM; D_m , gas kinetic diameter; D_p , pore diameter; dn/dt , molar gas permeation rate; m , gas molecular weight; E_a , energy barrier associated with pore crossing; k_B , the Boltzmann constant; T , absolute temperature; C_{surf} , areal density of adsorbed gas molecules; and μ_g , dynamic viscosity.

$$\Pi_{effusion}^* = \frac{1}{\sqrt{2\pi m k_B T}} \cdot \frac{\pi (D_p - D_m)^2}{4} = \Pi_{effusion} \left(1 - \frac{D_m}{D_p}\right)^2 \quad (6)$$

Note that Equation (6) assumes that all the gas impingement trajectories are perpendicular to the membrane, or that the angle of incidence $\theta = 0$, which is not realistic. The spatially uniform angle of incidence distribution of gas impingements $f_\theta(\theta) = 2\sin\theta\cos\theta$ derived from the Maxwell–Boltzmann velocity distribution was considered by Sun et al., and they carried out hit-and-miss Monte Carlo simulations to estimate the correction needed for $\Pi_{effusion}^*$.^[61] Later, Blankschtein and co-workers mathematically derived the exact solution based on $f_\theta(\theta) = 2\sin\theta\cos\theta$, and introduced the following approximation

$$\Pi_{effusion}^* = \Pi_{effusion} \left(1 - \frac{D_m}{D_p}\right)^3 \quad (7)$$

with a maximum absolute error of 2.2%.^[62] In fact, Equation (7) may still overpredict the effusive gas permeance because the trajectory of gas impingement onto the pore is not necessarily straight, and can be distorted by van der Waals interactions with the NATM surface.^[63] This further reduces the success rate of effusion because the gas molecules are generally attracted away from the pore. This effect is difficult to model analytically. However, inspired by Equations (6) and (7), the following semiempirical equation can be proposed

$$\Pi_{effusion}^* = \Pi_{effusion} \left(1 - \frac{D_m}{D_p}\right)^\alpha = \frac{1}{\sqrt{2\pi m k_B T}} \cdot \frac{\pi D_p^2}{4} \left(1 - \frac{D_m}{D_p}\right)^\alpha \quad (8)$$

where α is a gas-dependent parameter. Equation (8) can reproduce the following two limiting cases: (i) $D_m/D_p \rightarrow 0$ leads to $\Pi_{effusion}^* = \Pi_{effusion}$ (original effusion), and (ii) $D_m/D_p \rightarrow 1$ leads to $\Pi_{effusion}^* \rightarrow 0$ (nearly no effusion due to steric hindrance).^[63]

In addition to effusion from bulk gas, based on some molecular dynamics (MD) studies, the adsorption layer of the gas molecules on NATMs is generally considered as another important source of gas permeation through NATM pores.^[61,64] Intuitively, we expect that the gas permeation rate through a pore in NATMs via the surface pathway along the gas adsorption layer $(dn/dt)_{surf}$ should be proportional to the areal density of surface-adsorbed gas molecules C_{surf} , as well as to the circumference of the pore πD_p .^[65]

To derive the permeance per pore via the surface pathway $\Pi_{surf} = (dn/dt)_{surf}/p$ (note that $\Delta p = p$ because we consider the one-way permeation rate), a key quantity is the surface Henry's coefficient $H_{surf} = C_{surf}/p$, which is analogous to the Henry's law constant which describes the phase equilibrium between bulk gas and dissolved gas in a solvent. Note that H_{surf} is not necessarily constant as a function of bulk pressure p , depending on the adsorption isotherm used. The Langmuir isotherm is often invoked (see the Appendix).^[65–67] However, the Langmuir isotherm is typically used for microporous solids with relatively low external surface areas.^[68] NATMs typically have large external surface areas, and therefore, gas adsorption on NATMs may be better described by the Brunauer–Emmett–Teller (BET) theory.^[69] At room temperature or above, and at a moderate pressure < 10 bar, gas adsorption on a NATM surface is typically far from saturation.^[59] Therefore, treating H_{surf} as being pressure-independent would not lead to significant error under typical conditions encountered in membrane separations.

Based on the 2D version of the kinetic theory of gases, the permeance per pore via the surface pathway is given by^[63,65]

$$\Pi_{surf} = \sqrt{\frac{\pi k_B T}{2m}} D_p H_{surf} \exp\left(-\frac{E_{a,inj}}{k_B T}\right) \gamma_{trans} \quad (9)$$

where $E_{a,inj}$ is the energy barrier that a gas molecule needs to overcome to inject (inj) into the pore area from the NATM surface, and γ_{trans} is a correction factor that accounts for situations where some gas molecules injecting into the pore area cannot bend their trajectories to translocate (trans) through the pore. The origin of $E_{a,inj}$ is the absence of van der Waals interactions between a gas molecule and a NATM pore. The values of $E_{a,inj}$ and γ_{trans} are not readily obtained using analytical derivations. Instead, atomic-scale simulations are required to gain deeper insights. It is worth recognizing that surface contamination on NATMs may significantly affect both H_{surf} and the velocity distribution of the adsorbed gas molecules, and thereby affect the validity of Equation (9). Furthermore, Equation (9) was derived in the low areal pore density limit. For extremely highly porous NATMs, including graphyne, graphdiyne, or other 2D polymers, a certain deviation from Equation (9) is expected, but expressing this deviation analytically requires further confirmation using MD simulations.

The effusion pathway and the surface pathway can exist simultaneously, acting as two possible ways for gas molecules to approach NATM pores without much interference from each other.^[63] Comparing Equation (4) ($\Pi_{effusion} \propto D_p^2$) with Equation (9) ($\Pi_{surf} \propto D_p$), the surface pathway becomes increasingly dominant as D_p decreases, while effusion dominates when D_p is sufficiently large.

When the pore diameter D_p further decreases below $2D_m - 3D_m$, the Pauli repulsion from the pore rim atoms becomes significant, leading to an energy barrier (or activation energy) E_a associated with pore translocation. A straightforward way to predict the gas permeance per pore in this activated regime Π_{act} involves directly incorporating the energy barrier E_a into the expression for effusion (Equation (4)) as follows^[70–73]

$$\Pi_{act} = \Pi_{effusion} \frac{1}{2} \operatorname{erfc} \left(\sqrt{\frac{E_a}{k_B T}} \right) \quad (10)$$

where erfc is the complementary error function. Equation (10) assumes that the effusive impingement attempts from the bulk gas represent all the attempts to overcome the energy barrier for pore translocation, and that the trajectories of the gas molecules are not affected by atoms in the NATMs, except for hard-sphere collisions. Based on subsequent studies, it is generally accepted that the attempts to cross a pore with an energy barrier do not have one-to-one correspondence with the impingement attempts via the effusion pathway.^[59,65,67] Instead, the gas molecules approaching the pore via the effusion pathway, or the surface pathway, may remain in the pore periphery and adsorb to the pore after their permeation attempts are rejected, thereby forming a pore-associated state.^[59,74] This pore-associated state is typically accompanied by an energy minimum along the translocation trajectory.^[29,75] Therefore, it is expected that the gas permeation rate of activated translocation is proportional to the number of pore-associated gas molecules N_{pore} . Furthermore, the energy barrier E_a appears in an Arrhenius form in the equation to predict the activated gas permeation rate, because of the quasiequilibrium between the pore-associated state and the transition state (typically when the gas molecule is at the pore center) according to the transition state theory.^[76,77] Based on the discussion above, the gas permeation rate of activated translocation $(dn/dt)_{act}$ can be expressed as follows^[59]

$$\left(\frac{dn}{dt} \right)_{act} = k_{act} N_{pore} = A_{act} \exp \left(-\frac{E_a}{k_B T} \right) N_{pore} \quad (11)$$

where k_{act} and A_{act} are the rate constant and the prefactor of activated translocation, respectively (both in s^{-1}). Similar to the surface Henry's coefficient H_{surf} defined earlier, here, the pore Henry's coefficient H_{pore} can be defined as $H_{pore} = N_{pore}/p$. Accordingly, Equation (11) can be rewritten to predict the permeance per pore via activated translocation Π_{act} as follows

$$\Pi_{act} = k_{act} H_{pore} = A_{act} \exp \left(-\frac{E_a}{k_B T} \right) H_{pore} \quad (12)$$

Rigorously, ab initio or MD simulations are needed to predict the energy barrier E_a . As a simplification, Wang et al. proposed the following equation to predict E_a based on simple Lennard-Jones interaction potentials, relying on the assumption that the pore–gas interaction is dominated by the Lennard-Jones interactions between the gas molecule and all the pore edge atoms^[30]

$$E_a \approx \frac{\pi D_c}{a} 4\epsilon \left[\left(\frac{\sigma}{D_c/2} \right)^{12} - \left(\frac{\sigma}{D_c/2} \right)^6 \right] \quad (13)$$

where ϵ and σ are the Lennard-Jones parameters of the gas–pore edge interaction potential (coarse-graining the gas molecule as a single entity), D_c is the pore diameter defined by the distance between the centers of opposite pore edge atoms, and a is the distance between adjacent atoms on the pore rim ($\pi D_c/a$ is the number of pore edge atoms). For gas permeation, D_c and D_p are typically correlated as $D_p = D_c - (D_{vdw}/\sqrt{2})$, where D_{vdw} is the van der Waals diameter of the pore edge atoms.^[61] The $\sqrt{2}$ factor accounts for the approximation that half of the gas–pore edge collisions lead to deflection away from the pore.^[78] Note that the distance parameter σ in the Lennard-Jones potential is strongly correlated to the gas kinetic diameter D_m , and that D_c and D_p are strongly correlated. Therefore, in Equation (13), $\sigma/D_c \approx D_m/D_p$. In this way, D_m/D_p can be regarded as a dimensionless number in Equation (13).

To predict the prefactor A_{act} , Jiang et al. and Solvik et al. proposed using transition state theory (TST) based on statistical mechanics. Specifically

$$A_{act} = \frac{k_B T}{h} \exp \left(\frac{\Delta S^\ddagger}{k_B} \right) \quad (14)$$

where h is the Planck constant, \ddagger denotes the transition state, and ΔS^\ddagger is the entropy difference between the transition state and the pore-associated state.^[29,67] The entropy difference ΔS^\ddagger can be further decomposed into translational, rotational, and vibrational components.^[29] However, Auerbach, while studying the molecular jump dynamics in zeolites, pointed out that TST should be expressed in the following form to describe the barrier-jumping kinetics of a classical molecule over a certain distance^[77]

$$k_{act} = \frac{1}{2} \bar{v}^\ddagger \frac{\exp \left[-\frac{A(z^\ddagger)}{k_B T} \right]}{\int_{-\infty}^{z^\ddagger} \exp \left[-\frac{A(z)}{k_B T} \right] dz} = \frac{1}{2} \sqrt{\frac{2k_B T}{\pi m}} \frac{\exp \left[-\frac{A(z^\ddagger)}{k_B T} \right]}{\int_{-\infty}^{z^\ddagger} \exp \left[-\frac{A(z)}{k_B T} \right] dz} \quad (15)$$

where \bar{v}^\ddagger is the average velocity of the gas crossing the transition state, z is the translocation coordinate (or the vertical distance to the NATM plane), z^\ddagger is the coordinate of the transition state, and $A(z)$ is the Helmholtz free energy profile along the gas translocation trajectory through the pore. This expression was also reported by Frenkel and Smit to predict the rate of rare barrier-crossing events.^[79] Although Equations (14) and (15) were both derived using TST, the key difference between them lies in the expression for the velocity, or the frequency, moving away from the transition state. Equation (14) better describes the imaginary vibrational frequency of a transition state in an actual reaction, where the “velocity,” or the “length scale,” is not well defined. Equation (15) better describes molecular transport, where the velocity of barrier crossing can be well defined and predicted according to the Maxwell–Boltzmann velocity distribution.^[79] Note that Equation (15) involves free energy, whose calculation requires sampling the entire phase space. Free energy sampling methods in MD simulations, or direct evaluation of the canonical partition function, would be required to introduce real numbers in Equation (15).^[80]

Quantum tunneling is a special mechanism of gas permeation when a translocation energy barrier exists. It plays a dominant role

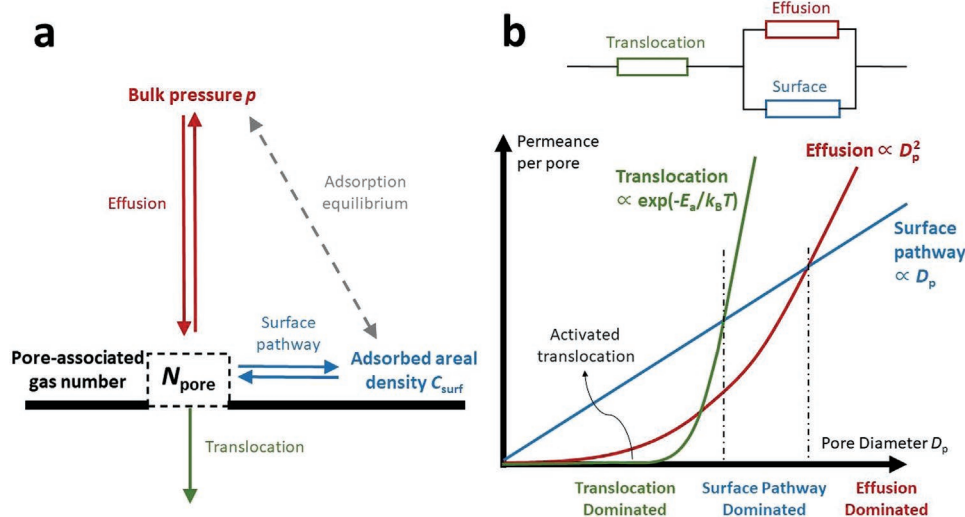


Figure 3. a) Schematic of incorporating effusion, surface pathway, and activated translocation into the same model. b) Top: transport resistances associated with translocation, effusion, and surface pathway represented in an electric circuit form; bottom: schematic of permeances per pore via different mechanisms as functions of pore diameter with different scaling.

for small gas molecules such as H_2 and He at low temperatures. Although quantum tunneling is a fundamentally different mechanism from thermally induced barrier climbing, the tunneling rate also depends strongly on the energy barrier height, because the transmission probability depends on the energy barrier E_a .^[81–85] For common operation conditions near room temperature, the contribution from quantum tunneling is very low.

The gas transport mechanisms discussed above, including activated translocation, surface pathway, effusion, and collective flow, are not mutually exclusive, and can occur simultaneously. More specifically, when $D_p < \lambda$, the first three mechanisms occur simultaneously, affecting gas permeance and selectivity at the same time. Blankschtein and co-workers proposed a reaction network model to incorporate the three mechanisms (Figure 3a), whose solution is shown as an analogous electric circuit in Figure 3b.^[63] Effusion and surface diffusion are parallel pathways to approach the pore and they are represented by parallel transport resistances. Translocation is the final step of pore crossing and its transport resistance is in series with the (effusion/surface) resistances in parallel. Note that the transport resistance R is defined as the inverse of the permeance per pore ($R = \Pi^{-1}$). Therefore, the total gas permeance per pore Π can be expressed based on its three contributions as follows^[63]

$$\Pi = \left(\frac{1}{\Pi_{\text{act}}} + \frac{1}{\Pi_{\text{effusion}}^* + \Pi_{\text{surf}}} \right)^{-1} \quad (16)$$

Because the three contributions to Π depend on D_p albeit with different scalings (Figure 3b, Equations (4), (9), and (12)), the gas permeation through a NATM pore transitions from the translocation-dominated regime (or the activated regime), to the surface-pathway-dominated regime, and then to the effusion-dominated regime, as D_p increases. Note that the surface-pathway-dominated regime may not exist, if the gas is weakly adsorptive, where the slope of the blue curve in Figure 3b would decrease accordingly.

Despite the progress made regarding the analytical description of gas permeation through NATM pores, significant challenges remain in terms of analytically describing the transition from the activated regime to the nonactivated regimes. When there is an energy barrier for pore translocation, the pore-associated state and the transition state are well defined in terms of their positions and energy landscapes. As the pore diameter increases and the energy barrier disappears, the pore-associated state and the transition state lose their physical meaning. The change is gradual and there is not a clear pore diameter value which separates the two regimes. This, in turn, makes it difficult to formulate a perfectly accurate mathematical description that covers the entire pore size range in a consistent manner. To address this challenge, atomic-scale simulations are useful to predict gas permeances more directly.

2.2. Simulations

The analytical descriptions discussed above only provide a general framework to predict gas permeances through NATM pores. In this regard, atomic-scale simulations have been carried out to estimate the gas permeances more precisely. Figure 4 summarizes the simulation results of gas permeation through NATM pores using molecular dynamics (MD) simulations,^[59,61,63,64,66,67,73–75,86–107] ab initio calculations,^[29,70,83,108–121] or a combination of both,^[72,82,122–137] as well as experimental results of gas permeation through individual graphene nanopores.^[60,138] The gases considered in Figure 4 include H_2 , He , H_2O , CO_2 , N_2 , O_2 , CH_4 , H_2S , Ar , SF_6 , ethane, and ethene. According to Equations (8), (9), and (15), the three contributions to the gas permeation per pore, Π_{effusion}^* , Π_{surf} , and Π_{act} , are all inversely proportional to \sqrt{m} , where m is the gas molecular weight. Therefore, in Figure 4a, the gas permeances per pore plotted on the y axis are multiplied by \sqrt{m} to offset the effect of the gas molecular weight. Furthermore, inspired by

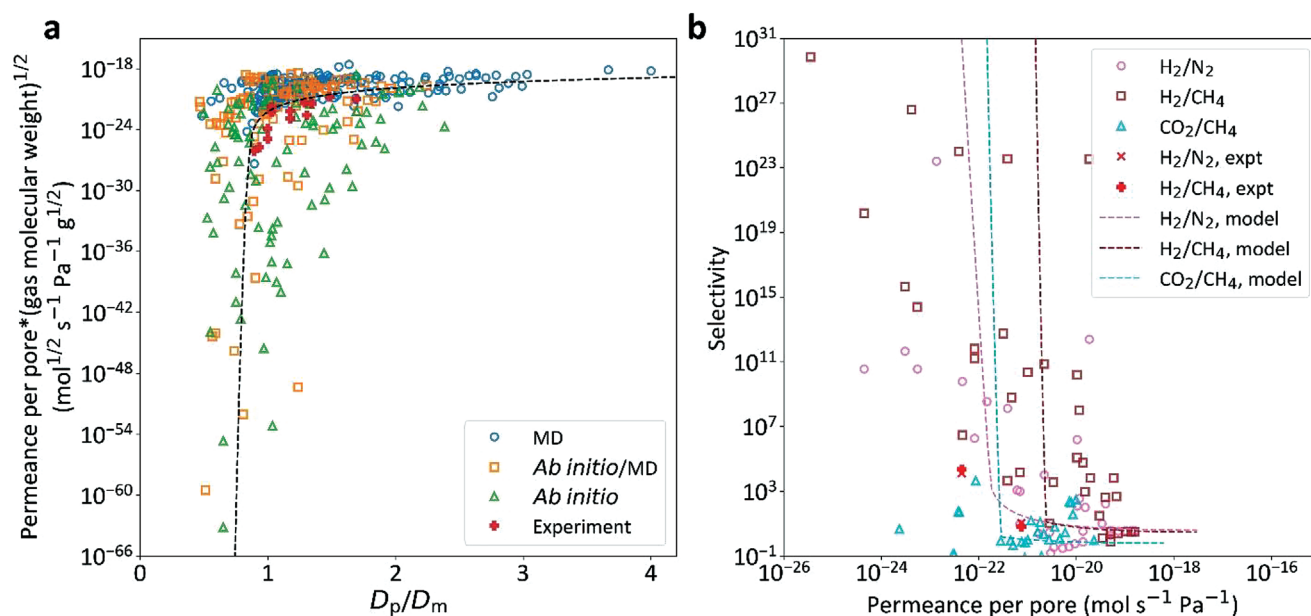


Figure 4. a) Compilation of simulation, analytical modeling, and experimental data of gas permeance per pore (normalized by the square root of the gas molecular weight) as a function of the pore diameter D_p (normalized by the gas kinetic diameter D_m). The simulation methods used include MD,^[59,61,63,64,66,67,73–75,86–107] *ab initio* calculations,^[29,70,83,108–121] and a combination of both.^[72,82,122–137] The experimental results are taken from ref. [138] and ref. [60]. b) Compilation of simulation, analytical modeling, and experimental data of H_2/N_2 , H_2/CH_4 , and CO_2/CH_4 selectivities as a function of the permeance per pore (permeance per pore of H_2 for the H_2/N_2 pair, of H_2 for the H_2/N_2 pair, and of CO_2 for the CO_2/CH_4 pair). Data sources are the same as in a). The dashed curves in a) and b) represent theoretical predictions based on the analytical model presented in Section 2.1.

Equations (8) and (13), it is reasonable to normalize the pore diameter D_p by the gas kinetic diameter D_m on the x axis because they are typically grouped together as a dimensionless number. As shown in Figure 4a, the \sqrt{m} -corrected gas permeance per pore generally increases as D_p/D_m increases, with a clear regime transition at $D_p/D_m \approx 1$. The high energy barrier associated with pore translocation when $D_p/D_m < 1$ leads to an exponentially reduced gas permeation. In contrast, the permeance increase when $D_p/D_m > 1$ is much milder. The general correlation presented in Figure 4a can be reproduced using the analytical descriptions discussed in Section 2.1 (dashed curve). To generate this curve, H_2 was chosen as the representative gas ($\varepsilon = 305.1 \text{ J mol}^{-1}$, $\sigma = 0.296 \text{ nm}$).^[139] The H_2 permeation contributed by the surface pathway was neglected because the physisorption of H_2 is very weak.^[64]

Regardless of the general trend, Figure 4a shows a considerable discrepancy between the simulation studies. In addition to the different simulation parameters used (e.g., exchange-correlation function in *ab initio* calculations or force field parameters in MD simulations), another important reason for the observed discrepancy is the variety of pore structures investigated. The NATM pores considered in Figure 4a include not only normal unterminated^[61,64] or hydrogen terminated pores^[29,59] encountered in 2D materials like graphene,^[83,86] MoS_2 ,^[118,127] hBN,^[95,115] and 2D polymers,^[111,137] but also pores functionalized with charged termination atoms, including nitrogen,^[75,82] oxygen,^[131] or fluorine,^[94,136] pores under mechanical strain,^[119,133] and pores in other novel NATM materials such as carbon nitride,^[129] silicene,^[110] phosphorene,^[116] or germanene.^[117] The gas transport behavior through a pore in NATMs depends strongly on the atomic composition of the

pore and its periphery, because these factors can significantly affect the energy landscape of the pore-associated state and the transition state.^[128] Simulation studies showed that pore functionalization groups effectively reduce the pore size.^[92,94,131] Further, functional groups which create dipoles or quadrupoles, including H_2S and CO_2 ,^[88,136] Multilayer membranes with overlapping pores in different layers can also be analyzed using the same framework as that used in the case of single-layer NATMs.^[122] For example, conical pores,^[107] asymmetric pores,^[104] and pores with tunable sizes^[101,103] have all been simulated for gas separations.

Figure 4b summarizes the selectivity-permeance trade-offs of H_2/N_2 , H_2/CH_4 , and CO_2/CH_4 separations, using the same dataset as in Figure 4a. Compared to Figure 4a, the datapoints in Figure 4b are less organized, and show low consistency with the model predictions (dashed curves). Generally, H_2/CH_4 exhibits the highest selectivity because it has the largest kinetic diameter difference (0.289 vs 0.38 nm), followed by H_2/N_2 (0.289 vs 0.364 nm), and then by CO_2/CH_4 (0.33 vs 0.38 nm).^[156] The large discrepancy observed in Figure 4b, especially in the high-selectivity region, indicates the importance of a high-accuracy evaluation of the translocation energy barrier E_a . A simple model like Equation (13) may not be sufficiently accurate.

In order to accurately estimate the energy barrier E_a associated with pore translocation, many *ab initio* calculations have been carried out.^[29,70,83,108–121] As shown by the green triangles in Figure 4a, *ab initio* calculations mainly target the lower end of the permeance-pore diameter relation, where activated translocation dominates the overall gas permeation. High E_a values

makes MD simulations unsuitable because it would take very long for a rare permeation event to occur.

However, according to Equation (12), the value of E_a itself is not enough to predict the gas permeance per pore. The main challenge is evaluating the prefactor A_{act} , which involves the entropy difference, or equivalently, the free energy difference between the transition state and the pore-associated state (Equation (15)). Evaluating the free energy requires sampling over phase space, which is inaccessible for ab initio calculations due to their high computational cost. To circumvent this problem, one method involves simply neglecting the effect of entropy and assuming a uniform A_{act} for all the gases considered through all pores. This method clearly led to considerable error. The transition state entropy of a gas molecule at the middle of a pore reflects the gas molecule's hindered translational, rotational, and vibrational degrees of freedom, which are expected to depend on both the gas considered and the pore structure. Jiang et al. took a step forward and used Equation (14) to estimate the entropy difference ΔS^\ddagger , which contributed a factor of 611 in terms of H_2/CH_4 selectivity. However, this method has not been widely adopted because of the extra computational resources required for its implementation. For similar reasons, and considering the large number of possible pore structures in NATMs,^[44] the fraction of pores studied by ab initio calculations is limited. This is certainly not optimal to advance a comprehensive understanding, especially when matching theoretical predictions with experimental results, because many different pore structures may exist in a membrane.

With the above in mind, it did not take long for researchers to recognize the need to exchange accuracy for efficiency. MD simulations rely on force field parameters and are less accurate than ab initio calculations. However, MD simulations are able to probe larger length scales, longer time scales, and more molecules, and therefore, allow more direct evaluations of gas permeances through NATM pores. As shown by the blue circles in Figure 4a, MD simulation results mainly cover the higher end of the permeance–pore diameter relation. Some studies carried out both ab initio and MD simulations and are marked as orange squares. As discussed above, MD simulations cannot effectively predict the gas permeance through a high-energy-barrier NATM pore by simply counting the number of permeation events. The typical time scale of an MD simulation is ≈ 10 ns,^[67,107] but it would take $\approx 10^4$ ns for one permeation event to occur, if $E_a = 0.3$ eV, given $\Delta p = 20$ bar.

Gas flow, and correspondingly, permeance and permeance per pore, can be directly predicted using MD simulations mainly using the following three mathematically equivalent methods: 1) Nonequilibrium, one-directional permeation. Here, gas molecules permeate from one compartment to an empty compartment through an NATM, and the initial permeation rate $(dN/dt)_0$ with maximum driving force can be derived by fitting the number of permeated gas molecules $N(t)$ using an exponential function (see the Appendix);^[73,89] 2) Equilibrium two-directional permeation. Here, gas molecules permeate between two compartments separated by an NATM with equal initial number of gas molecules inside. The trajectories of all

the gas molecules are recorded to evaluate the gas flow.^[61,63] A key assumption of this method is that gas permeation events are relatively rare such that gas permeation in one direction does not interfere with that in the opposite direction;^[61] 3) Repeatedly recording the time elapsed for the first permeation event t_1 to occur.^[59] According to the exponential distribution, the inverse of the averaged t_1 over many simulation runs is the initial permeation rate $(dN/dt)_0$.^[59] Although it is challenging for these MD simulation methods to evaluate the gas permeance through high-energy-barrier NATM pores, they highlighted the importance of the surface pathway when translocation is not rate-limiting.^[61,63,64,66] Furthermore, these MD simulation methods are essential in order to confirm and refine the analytical descriptions discussed in Section 2.1.^[59,106]

A useful way to predict the gas permeance per pore through a high-energy-barrier NATM pore using MD simulations is to artificially add a bias potential to force the gas molecule through the pore. A widely utilized technique is umbrella sampling, where a series of local harmonic bias potential wells are used to offset the high energy barrier.^[140] Umbrella sampling is a free energy sampling method and outputs the free energy profile $A(z)$ along the permeation coordinate. Umbrella sampling has been utilized in many studies to find the free energy profile of gas permeation through NATM pores, to analyze the effect of entropy, and to predict gas permeance per pore in the activated regime according to Equation (15).^[59,75,95,126,141] Note that the value of the energy barrier in MD simulations depends on the MD force field used, and is not as accurate as that in ab initio calculations. However, the free energy sampling method in MD simulations is still highly useful because it provides both energetic and entropic information about gas permeation.

Reviewing the development of simulation studies to model gas permeation through NATM pores, we note that the objective of these studies has become increasingly realistic. Early simulation studies aimed at showcasing the ultrahigh gas-separation properties of a few “example” nanopores. Later, the overall goal was to find the ideal pore structure to separate certain gas pairs. However, as the experimental datasets associated with gas permeation through NATMs began to grow in recent years, it is still challenging to match theoretical or simulation predictions to experimental results with high confidence. Fine-tuning the structure of a pore in NATMs is far more difficult experimentally than using simulations. In most cases, the NATM pores created experimentally have a pore size distribution (PSD) and it is difficult to control or characterize their edge terminations.^[142,143] In order to make the theoretical or simulation predictions consistent with the experimental results, the number of unknown parameters should be reduced to avoid overfitting. For example, given enough different pore structures and their corresponding permeances per pore, one could combine them to obtain any desired total gas permeance and selectivity. Therefore, casting simulation results in terms of analytical equations should be useful because it will help reduce the number of fitting parameters, thereby reducing computational cost. Additional details about matching theory with experiments will be discussed in Section 4.

3. Experiments

3.1. Perforation Strategies

In this section, we discuss the key experimental step that determines the gas-separation properties of NATMs: perforation.

3.1.1. Impermeability of NATMs

To date, most experimentally fabricated NATMs are based on graphene, including single-layer graphene (SLG), double-layer graphene (DLG), or multilayer graphene (MLG) because graphene membranes are much simpler to fabricate compared to other 2D materials. Mechanical exfoliation^[144] and chemical vapor deposition (CVD) growth^[145] are two major and mature ways of fabricating single- to few-layer graphene. For years, defect-free graphene has been regarded as gas impermeable because the gap in an aromatic ring in graphene is only 0.064 nm in diameter, which is much smaller than the kinetic diameter of the smallest gas molecule He (0.26 nm), leading to an almost insurmountable energy barrier to cross a graphene surface.^[35] The case is similar for other 2D materials with no pores. Bunch et al. experimentally showed that SLG is impermeable to He, Ar, and air by sealing a microchamber using SLG.^[34] Recently, Sun et al. significantly improved the detection limit of gas permeation through SLG, and showed that H₂ is an exception to the impermeability of SLG.^[36] In spite of being a larger molecule than He, H₂ exhibited noticeable permeance through defect-free SLG.^[36] The mechanism of H₂ permeation is different from the normal physical permeation of gases through NATM pores. It is hypothesized that H₂ first dissociatively chemisorbs on graphene ripples, forming sp³-bonded H adatoms. Then, these H adatoms flip to the other side of SLG with an energy barrier of 1.0 eV and recombine into H₂.^[36] In spite of the interesting mechanism, the H₂ permeance through defect-free SLG is too low for practical purposes.

The nearly impermeable characteristic of graphene and other atomically thin 2D materials to gases suggests that they need to be perforated in order to obtain practically meaningful gas permeances. The perforation process, or the pore generation process, is undoubtedly the key process that determines the gas-separation performance of an NATM. Because of their higher scalability than other methods, the most frequently used perforation strategies include ion beam bombardment (Figure 5a), oxidative etching (Figure 5b), and intrinsic defect formation during CVD (Figure 5c).^[146] Other less frequently utilized strategies include voltage pulse,^[60,147] electron beam etching,^[148] and CVD growth with a patterned substrate.^[149] Below, we will review the major perforation strategies one-by-one.

3.1.2. Ion Bombardment

The rationale of the ion bombardment strategy is straightforward—high energy ions hit the 2D materials and remove their atoms by collision. Celebi et al. used Ga-based and He-based focus ion beam (FIB) to perforate DLG and demonstrated the gas-separation capability of NATMs for the first time.^[150] The pore diameters in this study ranged from 7.6 nm to 1 μm, cov-

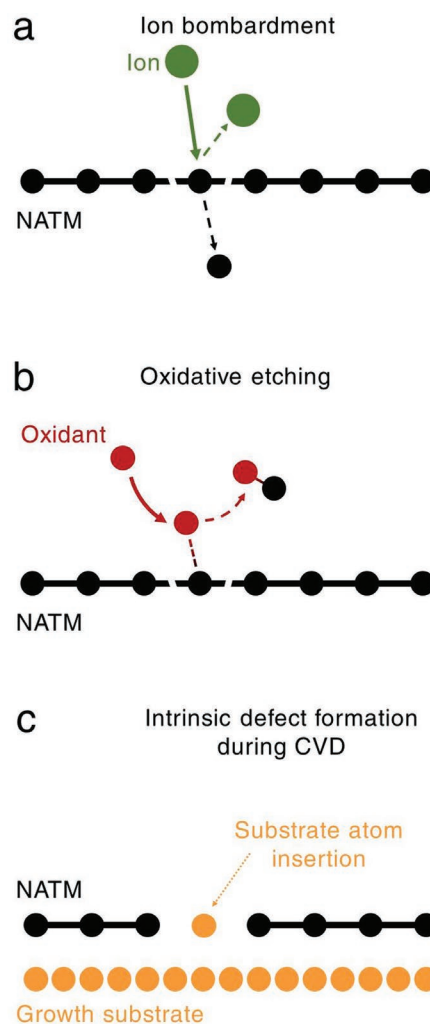


Figure 5. a) Schematic of ion bombardment for pore creation in NATMs. The energy required for bond breaking is contributed by the kinetic energy of the injecting ion (green). b) Schematic of oxidative etching for NATM perforation. The energy required for bond breaking is contributed by the chemical bonding between NATM atoms and the oxidant (red). c) Schematic of intrinsic defect formation in NATMs during chemical vapor deposition (CVD). Defects are created due to the insertion of substrate atoms into the NATM lattice.

ering the transition from the effusion-dominated regime to the collective flow regime. Because the pore diameters were much larger compared to the kinetic diameters of the gases tested, the selectivities did not exceed the Knudsen selectivities. Later, Ga⁺ ion beam was used to perforate DLG,^[151] triple-layer graphene,^[152] and single-layer tungsten disulfide,^[153] and yielded approximately Knudsen selectivities. Recently, ion bombardment is frequently used for pore nucleation. Liu et al. used He⁺ ion bombardment to perforate DLG.^[154] The areal pore density reached $6.7 \times 10^{15} \text{ m}^{-2}$ (average pore distance $L_D = 6.9 \text{ nm}$) when an irradiation dose of $10^{15} \text{ ions cm}^{-2}$ was used. In spite of the high areal pore density, the H₂ permeance through the perforated DLG was $\approx 3 \times 10^{-4} \text{ GPU}$ ($1 \text{ GPU} = 3.35 \times 10^{-10} \text{ mol m}^{-2} \text{ s}^{-1} \text{ Pa}^{-1}$), much lower than those through other NATMs or conventional polymeric membranes (Figure 6). This indicates that most of the defects created in

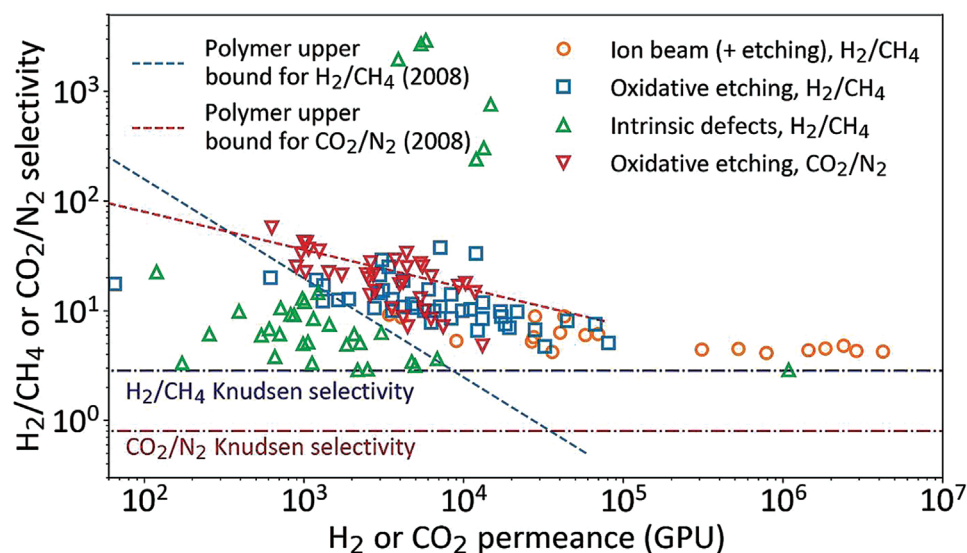


Figure 6. Compilation of experimentally measured H₂/CH₄ and CO₂/N₂ separation performances by NATMs in a selectivity-permeance Robeson plot. The experimental results are categorized according to the perforation methods used, including ion beam bombardment (some followed by additional chemical etching),^[150–154,156,157] oxidative etching,^[143,158–166] and intrinsic defect formation during CVD.^[62,143,149,159,160,164,167–171] The Robeson upper bounds for polymers are plotted assuming 1 μm thickness.^[11]

this study were so small (probably single-point or double-point vacancies) that the gas permeance through them was very low. This example shows that ion bombardment, due to the high controllability of its dose, is a good strategy to create small vacancies in defect-free 2D materials without further expanding the vacancies excessively. This feature allows the separation of pore nucleation and pore expansion, which is beneficial for narrowing the PSD in NATMs (see Section 3.2 for additional discussion). The threshold displacement energy associated with pore nucleation (≈ 20 eV for SLG)^[155] is higher than that associated with pore expansion (≈ 14 eV for SLG).^[148] In other words, pore expansion is kinetically faster than pore nucleation, due to the smaller number of broken chemical bonds required. As a result, if pore nucleation and pore expansion could occur simultaneously, pores nucleated earlier would become much larger than those nucleated later, leading to a wide PSD. Following this logic, Boutilier et al. used Ga⁺ ion bombardment to trigger pore nucleation in SLG and then expanded the pores by oxygen plasma.^[156] Similarly, Schlichting and Poulikakos nucleated pores in DLG by Ga⁺ ion bombardment and then expanded the pores by O₂ etching at 300 °C.^[157] Gas selectivities in both studies slightly exceeded the Knudsen selectivities.

3.1.3. Oxidative Etching

Oxidative etching has recently become a frequently used strategy to perforate 2D materials and to generate NATMs because of its low requirement for equipment and high scalability. So far, the etchants utilized to generate NATMs for gas separation include ozone (O₃), oxygen plasma, and O₂ at a high temperature. Koenig et al. used ultraviolet light to generate O₃ from air, which generated a handful of sub-nanometer pores in exfoliated DLG exhibiting a H₂/CH₄ selectivity $>10^4$.^[138] In spite of the low areal pore density, this study showed the high promise of the oxidative

etching method. O'Hern et al. used KMnO₄ in an acid solution to expand SLG nanopores nucleated by ion bombardment, and then used the resulting SLG membranes for ion separation and nanofiltration.^[142,172] Surwade et al. used oxygen plasma to etch SLG and obtained a high salt rejection rate and an impressive water permeability through the nanoporous SLG membranes.^[173]

Those studies inspired researchers to apply the oxidative etching methods to fabricate NATMs for gas separation. Huang et al. exposed CVD-grown SLG to O₃ at various temperatures ranging from 25 to 100 °C and improved the H₂/CH₄ selectivity to 17 while maintaining a H₂ permeance of 1.3×10^3 GPU.^[159] He et al. used oxygen plasma to generate nanopores in SLG with an areal density of $\approx 10^{16}$ m⁻² and obtained a CO₂/N₂ selectivity of 12 and a H₂/CH₄ selectivity of 16.^[143,160] Since then, O₃ and oxygen plasma treatment have been frequently reported to nucleate and expand pores in NATMs.^[158,162,164–166] Because these oxidative etchants can participate in both pore nucleation and pore expansion, the coupling between the two processes and the subsequent wide PSD have become a concern. To address this challenge, Zhao et al. developed a two-step procedure as follows. SLG was first exposed to oxygen plasma to create a high density of pore nuclei, and was then treated by O₃ for controllable pore expansion.^[161] This strategy to partially decouple pore nucleation and pore growth further improved the H₂/CH₄ selectivity to 29. In addition, O₃ treatment was shown to functionalize the pore edge and to shrink the pore size. Similarly, Huang et al. used a short burst of high-temperature O₃ for pore nucleation in SLG and then expanded the pores by O₂ at 200 °C, resulting in CO₂/N₂ selectivities of 24 and CO₂ permeances $\approx 10^4$ GPU.^[163] Further, in this study, the H₂/CH₄ selectivity was improved to 33, while a high H₂ permeance of 1.2×10^4 GPU was obtained. As shown in Figure 6, NATMs perforated by oxidative etching methods generally performed better than those perforated by ion bombardment. The oxidatively etched NATMs not only exhibited higher selectivities than

the Knudsen selectivities, but also surpassed the 2008 Robeson upper bound of polymeric membranes for H_2/CH_4 separation and CO_2/N_2 separation (assuming 1 μm thickness).^[11]

3.1.4. Intrinsic Defects

The third major perforation strategy is to utilize the defects formed during the CVD growth or the transfer process of 2D materials. Defects in CVD-synthesized 2D materials mainly consist of two types: nanometer-scale intrinsic defects and micrometer-scale large tears. The latter is not favorable for gas-separation purposes because such tears lead to nonselective collective gas flow. Nevertheless, large tears were difficult to avoid in the early stages of this research field when mechanical enhancement methods for NATMs had not been developed. Boutilier et al. studied the gas-separation properties of graphene with large tears and showed that the gas selectivity could be improved by stacking multiple graphene layers and by carefully engineering the gas transport resistance through the support that carried the graphene membrane.^[167] Unfortunately, the existence of large tears in NATMs limits the gas selectivity below the Knudsen selectivity.

Later, the development of mechanical enhancement methods prevented the formation of large tears and allowed the gas-separation properties of the nanometer-scale intrinsic defects to be measured (see Section 3.3 for a detailed discussion). Huang et al. showed that the intrinsic defects in CVD-grown SLG could yield a H_2/CH_4 selectivity of 22.^[159] Khan et al. synthesized SLG by CVD using benzene as the precursor, and the benzene-derived SLG exhibited a H_2/CH_4 selectivity of 8 and a H_2 permeance of 1152 GPU at 150 °C.^[168] Other researchers have also measured close to, or slightly higher, than the Knudsen selectivities through intrinsic defects in SLG.^[62,164,169] These results show that the intrinsic defects in graphene have the potential to be gas sieving.

In spite of the progress, the formation mechanism of the intrinsic defects was the least understood among the three perforation methods, and it led to low controllability and mediocre gas-separation performances. The intrinsic defects could form in three ways: i) in situ generation inside individual graphene single crystal domains during CVD growth,^[174] ii) imperfect merging of grain boundaries,^[175] and iii) oxidative etching by a trace amount of impurity.^[176] Rezaei et al. systematically studied the effect of the catalytic Cu substrate for graphene CVD growth and found that annealing the Cu substrates could increase the gas selectivities of the resulting SLG membranes while reducing their gas permeances.^[170] Kidambi et al. showed that the areal defect density in CVD-grown SLG could be increased by reducing the CVD temperature.^[177,178] Recently, Strano and co-workers showed that the areal density of the intrinsic defects in SLG can be increased by increasing the graphene growth rate, reducing the CVD temperature, and reducing the concentration of O_2 impurity.^[171] The results were consistent with the theoretical study carried out by Wang et al.,^[179] where most intrinsic defects were nucleated inside individual graphene domains due to the random insertion of Cu adatoms into the graphene growth front (Figure 5c). The defects were then expanded by O_2 impurity to form gas permeable pores.

Guided by this mechanism, nanoporous SLG membranes with high H_2/CH_4 selectivities >2000 and H_2 permeances >4000 GPU were fabricated.^[171] The underlying reason for the high gas-separation performance resulting from the intrinsic defects is the more complete decoupling between pore nucleation and pore expansion compared with the oxidative etching methods. It is difficult to prevent strong oxidants, such as O_3 and oxygen plasma, from inducing pore nucleation and pore expansion simultaneously. This imperfect decoupling leads to a dilemma: the pore density cannot be significantly increased by increasing the energy intensity of oxidative etching, because that will further expand the pores and cause the gas selectivity to decrease.

In general, currently, ion bombardment, oxidative etching, and intrinsic defect formation in CVD are three major ways of pore nucleation, while oxidative etching plays a dominant role in pore expansion. Voltage pulse^[60,147] and electron beam etching^[148] could create pores in 2D materials with high precision in terms of pore size, but the areal pore densities were limited for these methods. CVD synthesis on patterned substrates could generate NATMs with high porosity by preventing 2D materials from growing over the pattern,^[149,180] but the pores were generally too large for gas sieving. In fact, fabricating and uniformly dispersing sub-nanometer particles on a substrate is, by itself, a very challenging problem. Apart from the perforation strategies discussed above, direct bottom-up synthesis of 2D polymers is a highly promising route.^[181,182] In fact, intrinsically nanoporous 2D polymers such as graphdiyne are regarded as “the ultimate membrane” due to their ultrahigh pore density and atomic thickness.^[128,183] The relatively low mechanical strength and its defect-free synthesis are two major challenges for those 2D polymers to serve as effective gas-separation membranes, but they may be overcome by a good supporting layer, as will be discussed in Section 3.3.

3.2. Pore Size Distribution

What determines the gas selectivity of a NATM is the sizes of its pores. Ideally, all the pores are of the same size and are highly gas selective. In this case, the PSD is a degenerate distribution for discrete pore sizes, or is a delta function for continuous pore sizes. However, as shown in Figure 7a,b, pores in NATMs created by top-down etching-based methods typically have a wide PSD which shows a long right tail (right-skewed).^[142,143,163,172] The right-skewed PSD is usually fitted to a log-normal distribution function (see the Appendix). The long right tail of the PSD is unfavorable for a high gas-separation performance. In spite of their low fraction among all the pores, the large pores in the right tail can dominate the overall gas permeance and are less gas selective.^[184] In order for the entire NATM to exhibit a high gas selectivity, the right tail needs to be kept short. As a result, most of the pores are too small to contribute any gas permeance, leading to a trade-off between permeance and selectivity. A wider PSD lowers the upper limit of the permeance-selectivity trade-off.

Unfortunately, narrowing the PSD of NATMs has been challenging, because, currently, most pores in NATMs are created by top-down etching methods, which are random processes by

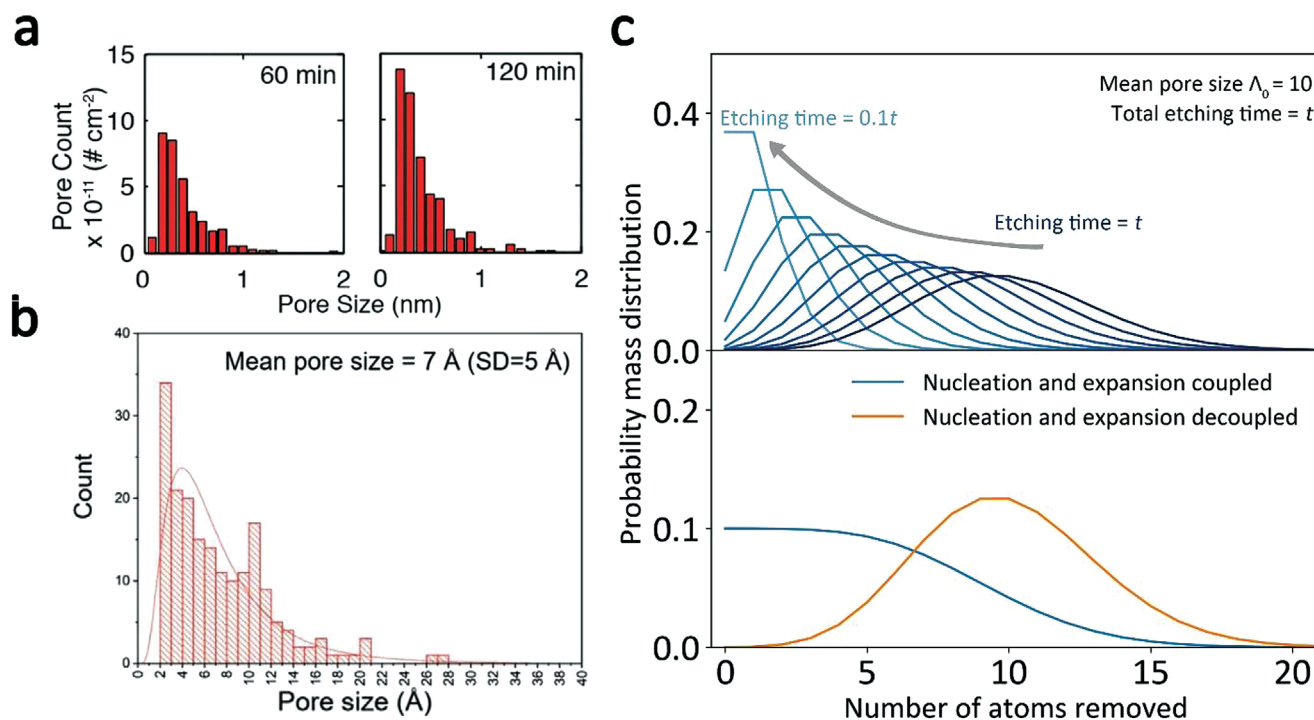


Figure 7. a) Distribution of pore diameters in a single-layer graphene membrane after 60 and 120 min of acidic KMnO_4 oxidation following ion bombardment. Reproduced with permission.^[142] Copyright 2014, American Chemical Society. b) Distribution of pore diameters in a single-layer graphene membrane etched by oxygen plasma for 1 s. Reproduced with permission.^[143] Copyright 2020, Wiley-VCH. c) Illustration of effect of the coupling between pore nucleation and pore expansion on the pore size distribution. The top panel shows 10 pore size distributions (PSDs) with etching time ranging from $0.1t$ to t (t is the total etching time). These PSDs are averaged to obtain the blue curve in the bottom panel. The orange curve is the PSD if all pores are etched for time t .

nature. In order to narrow the PSD of NATMs, decoupling pore nucleation and pore expansion has been a useful strategy, as discussed in Section 3.1.^[161,163] If pore nucleation and pore growth occur simultaneously, the overall PSD $f_{D_p}(D_p; t)$ resulting from a total etching time of t is a convolution of the probability density function of pore nucleating at time τ , $f_{\text{nuc}}(\tau)$, and the probability density function of pore size after the remaining time for pore expansion $t - \tau$, $f_{\text{expan}}(D_p; t - \tau)$, that is^[185]

$$f_{D_p}(D_p; t) = \int_0^t f_{\text{nuc}}(\tau) f_{\text{expan}}(D_p; t - \tau) d\tau \quad (17)$$

A reasonable $f_{\text{nuc}}(\tau)$ is the uniform distribution, assuming that the etchant concentration is constant over time and that the sites for pore nucleation are far from saturation. In that case

$$f_{\text{nuc}}(\tau) = 1/t \quad (18)$$

Consider the expansion of a pore due to etching, starting from a point defect. If the etching rates of all the under-coordinated pore edge atoms are the same (which is nearly true for graphene),^[44] the resulting PSD in terms of the number of atoms etched M follows a Poisson distribution (note that the PSD is represented here by the discrete probability mass function P_{expan} , because M is a discrete variable), that is^[186]

$$P_{\text{expan}}(M) = \frac{\Lambda^M e^{-\Lambda}}{M!} \quad (19)$$

where Λ is the mean pore size in terms of the number of atoms etched. Note that M does not include the originally removed atom in the point defect and that M may be zero. The mean pore size Λ can be assumed to be a linear function of the remaining etching time $t - \tau$. $\Lambda = r(t - \tau)$, where r is the pore expansion rate. Convoluting Equations (18) and (19), the overall PSD $P_M(M; t)$ can be expressed as follows^[185]

$$\begin{aligned} P_M(M; t) &= \int_0^t f_{\text{nuc}}(\tau) P_{\text{expan}}(M; t - \tau) d\tau = \int_0^t \frac{1}{t} \frac{[r(t - \tau)]^M e^{-r(t - \tau)}}{M!} d\tau \\ &= \frac{1}{rt \cdot M!} \int_0^t x^M e^{-x} dx = \frac{1}{rt \cdot M!} \Gamma(M + 1, rt) \end{aligned} \quad (20)$$

where $\Gamma(M + 1, rt)$ is the lower incomplete gamma function. Note that in Equation (20), rt can be combined as a single variable: $\Lambda_0 = rt$, and Λ_0 can be regarded as the mean pore size if pore nucleation and pore expansion are completely decoupled ($\tau = 0$ for all the pores). Therefore, the overall PSD with coupled pore nucleation and pore expansion (with Poisson kinetics) can be rewritten from Equation (20) as follows

$$P_M(M; \Lambda_0) = \frac{1}{M!} \frac{\Gamma(M + 1, \Lambda_0)}{\Lambda_0} \quad (21)$$

Table 1. Comparison between the mean pore size and the skewness of the pore size distributions derived when pore nucleation and pore expansion are decoupled or coupled. Each column corresponds to a certain Λ_0 value (the product of the pore expansion rate r and the etching time t).

Mean pore size w / decoupling Λ_0	1	2	4	6	8	10	15	20	30
Mean pore size w / coupling	0.5	1	2	3	4	5	7.5	10	15
Skewness w / decoupling	1.00	0.71	0.50	0.41	0.35	0.32	0.26	0.22	0.18
Skewness w / coupling	1.68	1.30	0.99	0.82	0.70	0.62	0.47	0.39	0.28

Equation (21) has the following important implications. First, as shown in Table 1, the mean pore size (in terms of the number of atoms etched) doubles when pore expansion is completely decoupled from pore nucleation, given the same etchant dose. Second, the right-skewness of the PSD is reduced when pore nucleation and pore expansion are decoupled. Therefore, decoupling pore nucleation and pore expansion shortens the right tail in the PSD and improves the gas-separation performance of NATMs. Finally, if pore nucleation and pore expansion occur simultaneously due to oxidative etching, the resulting PSD is determined by the product of the pore expansion rate r and the etching time t ($\Lambda_0 = rt$). Note that this prediction is based on the assumption that pore nucleation is temporally uniform (Equation (18)). If the etchant concentration changes over time,^[165,166] the resulting PSD also depends on the concentration profile of the etchant.

When oxidative etching is used for pore nucleation, simultaneous pore expansion is inevitable. In order to maintain a high gas selectivity, the pores cannot be expanded excessively during the pore nucleation process, which indicates that the Λ_0 value should be restricted (Equation (21)). Practically, a stronger etchant at a higher etching temperature is preferred. This is because to nucleate more pores, the pore nucleation rate r_{nuc} should be as large as possible. Because the energy barrier associated with pore nucleation $E_{\text{a,nuc}}$ is typically greater than that associated with pore expansion $E_{\text{a,expan}}$ ($E_{\text{a,nuc}} > E_{\text{a,expan}}$),^[148] the pore nucleation rate r_{nuc} is typically lower than the pore expansion rate r ($r_{\text{nuc}} < r$). In fact, according to the Arrhenius equation, it follows that

$$\frac{r_{\text{nuc}}}{r} \propto \exp\left(-\frac{E_{\text{a,nuc}} - E_{\text{a,expan}}}{k_{\text{B}}T}\right) \quad (22)$$

Equation (22) suggests the following two strategies to increase r_{nuc}/r . First, strong oxidants such as O_3 or O_2 plasma can attack both triply bonded lattice atoms and doubly or singly bonded pore edge atoms with high reactivities and low energy barriers, thereby reducing the difference between the two energy barriers. Second, a high etching temperature increases the denominator in the exponent in Equation (22), and therefore, increases r_{nuc}/r . Recall that $\Lambda_0 = rt$. Because Λ_0 is restricted for a high gas selectivity and r is large due to the use of a strong etchant and a high etching temperature, the etching time t should be short. As discussed in Section 3.1, Huang et al. utilized the combination of a strong etchant (O_3), high etching temperature (250–290 °C), and short etching time (millisecond pulse) to obtain high gas-separation performances using SLG membranes.^[163] Hsu et al. claim that the energy barriers for nanopore nucleation and expansion are similar for O_3 (≈ 1 eV), which increases r_{nuc}/r according to

Equation (22) and yields a higher pore density and higher gas permeances.^[165]

In spite of the strategy discussed above, pore nucleation triggered by oxidative etching cannot be completely decoupled from pore expansion. Ion bombardment and intrinsic defect formation are two alternative methods that may better enable the decoupling. As discussed in Section 3.1, a high density of very small defects can be created in SLG using ion bombardment.^[154] The nucleation of intrinsic graphene defects during CVD is caused by the random insertion of Cu atoms into the graphene growth front.^[179] The time window for subsequent pore expansion closes when the growth front moves past the defect, leading to decoupled pore nucleation and pore expansion.^[171]

Decoupling pore nucleation and pore expansion is certainly a useful strategy, but it does not eliminate all the problems associated with the PSD in NATMs. A misconception is that if pore nucleation and pore expansion are completely decoupled, the resulting PSD would be very narrow, or in other words, that the broad PSDs observed in NATMs are solely caused by the convolution between pore nucleation and pore expansion. This is unfortunately not the case. As shown in Table 1, the right-skewness of the PSD persists even if pore nucleation and pore growth are completely decoupled. This is a manifestation of the nature of etching sub-nanometer scale pores using a top-down approach. According to the central limit theorem, the relative standard deviation of the pore size M scales as $1/\sqrt{M}$ (assuming independent etching events). For sub-nanometer scale pores, the values of M are small, leading to wide PSDs.

To completely circumvent the problems caused by wide PSDs, other strategies need to be pursued. Two potential strategies are discussed below: i) The first strategy involves postsynthetic tuning of the PSD. For example, interfacial polymerization has been used to preferentially block larger pores to alleviate the detrimental effect of the large tears.^[172,187,188] Recently, Strano and co-workers showed that pyrene-based molecules can strongly adsorb onto graphene surfaces and partially block the graphene pores, with the larger pores blocked to a larger extent;^[171] ii) The second strategy involves the bottom-up synthesis of 2D polymers like graphyne and graphdiyne.^[128,183] Wide PSDs will no longer exist because the nanoporous 2D polymers naturally contain uniform porous structures, if large tears and imperfect grain boundaries can be avoided.

3.3. Functional Supporting Layers

3.3.1. Mechanical Reinforcement

Although NATMs are typically strong on a microscopic scale, they are macroscopically fragile, especially when they come in

contact with high-surface-tension liquids during transfer.^[189,190] In this regard, a supporting layer can mechanically strengthen the NATM and prevent large tears from forming. Because an NATM has a higher probability to rupture when it is suspended over a larger hole or a wider trench,^[191] NATMs have been transferred to substrates with arrays of holes to increase the total membrane area.^[159] In this case, mechanical enhancement of NATMs is still important because a single tear in one of the suspended areas would cause the entire membrane to fail.

The supporting layers for NATMs should preferably be mechanically robust, chemically stable, and have much higher gas permeances than those of the NATMs. Consider vertically stacking L membrane layers to separate gas 1 from gas 2 (gas 1 is more permeable than gas 2). Assume that the permeance of gas 1 through each membrane layer j ($j = 1, 2, \dots, L$) is K_j , and that the selectivity of each membrane layer is S_j . If no interlayer resistance exists, the overall permeance K_{tot} can be calculated by adding up all the transport resistances in series, that is

$$K_{\text{tot}} = \left(\sum_{j=1}^L K_j^{-1} \right)^{-1} \quad (23)$$

Further, the overall selectivity of the composite membrane S_{tot} is given by

$$S_{\text{tot}} = \frac{\sum_{j=1}^L S_j K_j^{-1}}{\sum_{j=1}^L K_j^{-1}} \quad (24)$$

Therefore, if the supporting layer has a lower, or comparable, gas permeance relative to that of the NATM, it will significantly affect the overall permeance and selectivity of the composite membrane.

Even if the supporting layer is highly gas permeable, it could still affect the overall gas permeance due to the existence of interlayer resistance. A straightforward example of interlayer resistance is that no gas can pass through the impermeable portion of the supporting layer via the interface between two layers. As a result, the pore size and porosity of the supporting layer can further affect the gas permeance by modulating the interlayer resistance.^[167] Inside polymeric membranes, gas molecules can diffuse laterally to access the pores in the support. On the other hand, an NATM leaves no pathway for gas molecules to diffuse laterally “inside” the membrane.^[34] Therefore, the local interlayer transport resistance becomes infinitely large, and the NATM’s effective area can be regarded as the open area of the support.

The most frequently used materials as mechanical reinforcement layers for NATMs include nanoporous carbon (NPC, Figure 8a) and carbon nanotubes (CNT) (Figure 8b). Generally, the gas permeance of the functional supporting layer is negatively correlated with its mechanical strength, because a high gas permeance requires the presence of large pores in the

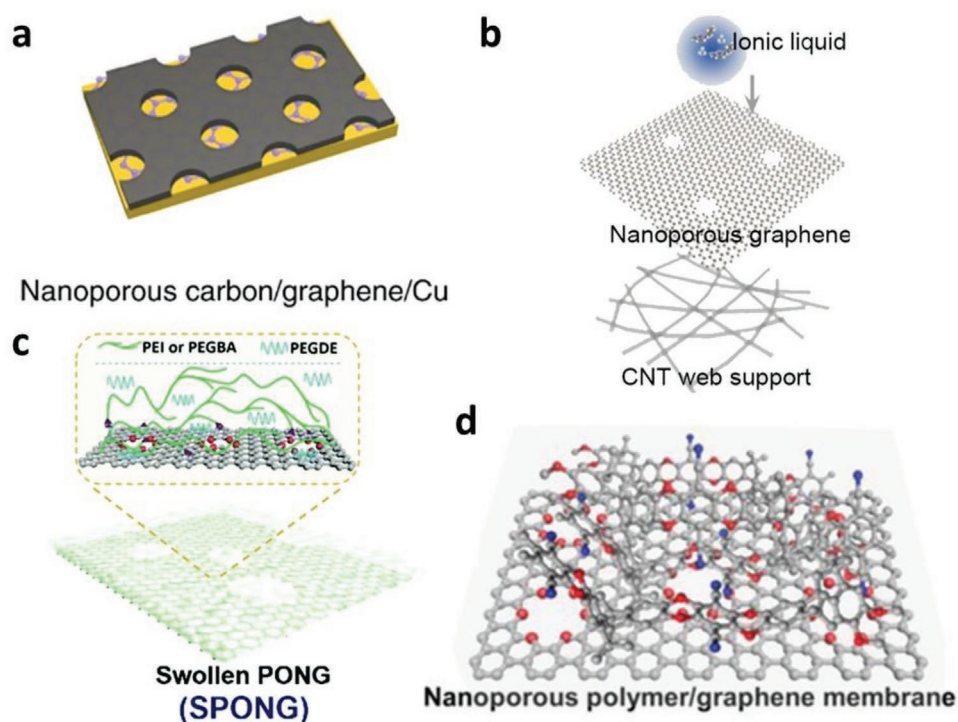


Figure 8. a) Schematic of SLG supported by a nanoporous carbon film during graphene transfer. Reproduced under the terms of the CC-BY Creative Commons Attribution 4.0 International license (<https://creativecommons.org/licenses/by/4.0/>).^[159] Copyright 2018, The Authors, published by Springer Nature. b) Schematic of SLG supported by a carbon nanotube web, which also serves as a host for ionic liquid coating. Reproduced with permission.^[158] Copyright 2020, American Chemical Society. c) Schematic of oxygen-functionalized single-layer graphene (ONG) grafted with polyethylenimine (PEI) or poly(ethylene glycol)-bisamine (PEGBA). The grafted polymer was then swollen by poly(ethylene glycol) dimethyl ether (PEGDE) oligomer. Reproduced with permission.^[160] Copyright 2019, The Royal Society of Chemistry. d) Schematic of SLG membrane hosting polymer with intrinsic microporosity (PIM-1). Reproduced with permission.^[143] Copyright 2020, Wiley-VCH.

material, which in turn weakens its mechanical properties. As illustrated in Figure 8a, the NPC supporting layer contains a high density of nanochannels that allow fast gas permeation.^[159] The NPC layer can be synthesized by the pyrolysis of phase-separated poly(styrene)–poly(4-vinylpyridine) (PS–P4VP) with carbohydrates.^[192] Huang et al. first implement this material for the mechanical enhancement of SLG.^[159] The NPC layer was 100 nm thick and had 20–30 nm sized channels. The gas permeance through the NPC layer reached 5.7×10^6 GPU, a much higher value than that through the nanoporous SLG, and therefore, the NPC layer only served as a mechanical support. A CNT web can play a similar role as the NPC layer in terms of protecting NATMs.^[164] Yang et al. protected SLG membranes using a network of single-walled carbon nanotubes and obtained robust salt rejection and nanofiltration performances.^[193] Guo et al. used the CNT web to host ionic liquids and significantly improved the CO_2/N_2 selectivity (Figure 8b).^[158]

3.3.2. Gas-Separation Performance Enhancement

Apart from providing mechanical support, the supporting layer can also be functionalized to improve the gas selectivity through NATMs. In other words, the supporting layer can be gas selective by itself. Equation (24) shows that the overall selectivity S_{tot} is a weighted average of the selectivities of each membrane layer, with the weight corresponding to the inverse permeance of each layer. This indicates that the overall selectivity S_{tot} cannot exceed the maximum of all the individual selectivities if no interlayer resistance exists. However, for NATMs, having an interlayer resistance is not rare, because the gas transport resistance through an NATM is governed by its interface. An extreme example is stacking two porous graphene layers without any overlapping pores. In this case, the overall gas permeance would be zero because the gas molecules cannot penetrate between the two stacked graphene layers. In other words, the interlayer transport resistance is infinitely large.

Polymers have been utilized as functional layers on NATMs to enhance their gas-separation performances (Figure 8c,d). Many polymeric materials are highly permselective by themselves, and have been used to improve the performance of NATMs with relatively low gas selectivities.^[149,152] In these studies, NATMs could be viewed as supporting layers for ultrathin polymeric membranes. Furthermore, synergistic effects could be observed if the NATM pores were coupled to the polymer chains, giving rise to additional interfacial transport resistance. In this case, Equation (24) is not valid and the overall selectivity of a composite membrane can exceed the selectivity of each individual membrane layer. For example, He et al. grafted CO_2 -philic polymers on porous SLG (Figure 8c)^[160] or coated polymer with intrinsic microporosity (PIM-1) on SLG (Figure 8d).^[143] The interaction between the polymer chains and the graphene pores led to significantly enhanced CO_2/N_2 selectivities >30 .

In summary, the functional supporting layers are essential for the overall gas-separation performance of NATMs. For potential large-scale applications of NATMs in the future, the role of the supporting layer will become increasingly relevant. In addition, mechanical enhancement will be required for

the implementation of more fragile but highly promising 2D polymer membranes.

4. Matching Theory with Experiments

In this section, we will discuss in detail the progress made in matching the theoretical predictions of gas permeation through NATMs with the experimental results. When gas permeation is governed by collective flow or effusion, it is straightforward to model the experimentally measured gas permeances and selectivities using analytical expressions. For example, Celebi et al. used Equations (1) and (4) to model the transition between the collective gas flow to effusion.^[150] Later, gas permeation through NATMs exhibiting below, or close to, Knudsen selectivities was successfully modeled based on effusion or collective flow.^[151–153,167] Subsequently, Equations (6) and (8) describing the effusion mechanism corrected by the steric effect were used to explain gas selectivities which are slightly higher than the Knudsen selectivities, allowing estimations of the average pore size.^[62,156]

However, as the size of the experimentally created pores further decreased, the resulting significant gas sieving and high selectivities could no longer be modeled or understood well solely using analytical equations, without the assistance of simulations. The problem was still tractable when the number of pores in an NATM was very small. Koenig et al. and Wang et al. created graphene membranes that contained only one to three nanopores, which showed high H_2/CH_4 and CO_2/CH_4 selectivities $\approx 10^4$.^[60,138] The small number of pores in the membranes allowed theorists to scan through a list of pore structures and to propose potential candidates.^[59,75,89]

For practical purposes, NATMs containing large numbers of pores were fabricated. However, the existence of PSDs greatly complicates the problem, and makes matching theory with experiments much more challenging. Note that the goal is to fit theoretical predictions of gas permeation through nanopores to the experimental data, and to predict the PSD in an NATM. Experimentally, the PSD in an NATM can be probed using high-resolution microscopy imaging over a scanning area of $>10^4 \text{ nm}^2$.^[142,160,167] Nevertheless, theoretical fitting is still an important tool to understand the PSD because a PSD acquired from microscopy imaging may not be equivalent to the actual effective PSD in a gas permeation measurement. First, pores in 2D materials may expand or merge under electron irradiation or thermal treatment.^[194] Second, the pore-edge termination group may be removed by electron beam, thereby affecting the effective pore size.^[163] Last, NATMs are prone to surface contamination during gas permeation testing, but unfortunately, the effect of surface contamination on the pores is typically not probed using microscopy imaging.^[195]

The complexity associated with PSDs indicates that the theoretical modeling of gas permeation through NATMs requires simplification. Assume that we have full knowledge of the permeance per pore Π as a function of the gas molecule i , the temperature T , and the pore structure (represented by the pore diameter D_p). Note that a single D_p value may correspond to multiple pore structures. Furthermore, the pore diameter may not even be a well-defined variable for nanopores because the

nanopores may not be circular. However, for simplicity and mathematical clarity, we choose to represent the pore structure by its pore diameter, which is a continuous variable. Another assumption made is that Π is independent of pressure p , which is a valid assumption in the low-pressure regime near ambient conditions. Note that in practice, we do not yet have full knowledge of Π as a function of i , T , and D_p , although this is certainly the goal of theorists.

Assuming that Π is known completely, it can be expressed as follows

$$\Pi = \Pi(D_p, i, T) \quad (25)$$

Using Equation (25), the theoretically predicted permeance $\hat{K}(i, T)$ (on an areal basis) for gas i at temperature T through an NATM with areal pore density ρ and PSD f_{D_p} can be expressed as follows

$$\hat{K}(i, T) = \rho \int_{D_p}^{+\infty} f_{D_p}(D_p; T) \Pi(D_p, i, T) dD_p \quad (26)$$

where in Equation (26) we have allowed f_{D_p} to depend on the temperature T . Experimentally, an NATM yields the permeances of multiple gases measured at multiple temperatures, $K(i, T)$. Then, the objective of the theoretical fitting is to minimize the least squared absolute error between $\hat{K}(i, T)$ and $K(i, T)$, yielding predictions for the PSD $f_{D_p}^*$ and for the pore density ρ^* . Specifically

$$\{f_{D_p}^*(D_p; T), \rho^*\} = \underset{f_{D_p}(D_p; T), \rho}{\operatorname{argmin}} \sum \left[\hat{K}(i, T) - K(i, T) \right]^2 \quad (27)$$

where $\operatorname{argmin} f(x)$ (argument of the minimum) is a function which gives back the parameter values x^* that minimize the objective $f(x)$.

Because the permeances of different gases may differ by several orders of magnitude, an alternative minimization objective is the least squared relative error, that is

$$\{f_{D_p}^*(D_p; T), \rho^*\} = \underset{f_{D_p}(D_p; T), \rho}{\operatorname{argmin}} \sum \left[\frac{\hat{K}(i, T)}{K(i, T)} - 1 \right]^2 \quad (28)$$

Considering the total number of different gases i tested n_i and the total number of different temperatures T tested n_T , the total number of experimental datapoints is $n_i n_T$. On the other hand, in theory, the number of unknown parameters needed to fully describe a PSD is infinitely large because of the many possible pore structures. One simplification is to describe the PSD using a simple log-normal distribution function, which requires two unknown parameters (Equation (34), Appendix). Note that the temperature dependence of the PSD implies that two unknown parameters are required for each temperature, leading to a total of $2n_T + 1$ unknown parameters (including ρ). It seems that if $n_i > 3$, the number of experimental datapoints exceeds the number of unknowns and the optimization problem (Equations (27) or (28)) becomes tractable. Unfortunately, we do not have full knowledge of Π and cannot express $\Pi = \Pi(D_p, i, T)$ without any unknown fitting parameters (e.g., energy barrier E_a , prefactor A_{act} , and pore Henry's coefficient

H_{pore} in Equation (12)). Because each pore size has its own expression of Π and its own unknown parameters, the total number of unknowns would explode, thereby making the theoretical fitting virtually intractable.

To make the fitting possible, three simplification strategies have been used to date. The first strategy is to generate the PSD using simulation tools. Blankschtein and co-workers developed a Kinetic Monte Carlo (KMC) algorithm that outputs a PSD, while using a single parameter, the etching time t , as the input.^[44,184] In this way, t becomes the one-degree-of-freedom representation of the PSD, thereby reducing the number of unknown parameters. The etching time t was fitted to minimize the error of the selectivities between H_2 , CO_2 , and CH_4 in ref. [143], and the fitted etching time t^* was found to be an increasing function of the measurement temperature. This important finding suggests that the pore sizes in an NATM effectively expand when the temperature increases, which is due to the desorption of surface contaminants from the NATMs and the corresponding attenuation in pore clogging.^[171,184]

The second strategy is to assume homogeneous pore sizes, or equivalently, that the PSD is a delta function. This is not necessarily a bad assumption because when the entire pore ensemble is highly gas selective, the majority of the overall permeance is contributed by a small fraction of large pores.^[184] These large pores may be well represented, on average, by a single pore size D_p . Following this assumption, Equation (26) can be simplified as follows

$$\hat{K}(i, T) = \rho \Pi(D_p(T), i, T) \quad (29)$$

If we further assume activated gas transport (Equation (12)), Equation (29) can be further simplified as follows

$$\hat{K}(i, T) = \rho A_{\text{act}} H_{\text{pore}} \exp \left[-\frac{E_a(D_p(T), i)}{k_B T} \right] = A_{\text{tot}} \exp \left[-\frac{E_a(D_p(T), i)}{k_B T} \right] \quad (30)$$

where A_{tot} is the product of all the unknown parameters multiplying the exponential term. Note that the energy barrier E_a is a function of D_p and gas type i . Due to the exponential dependence in Equation (30), it is convenient to take the natural logarithm of Equation (30), and then plot $\ln[K(i, T)]$ as a function of $-1/k_B T$, where the slope of the resulting line corresponds to the apparent energy barrier $E_a^*(i)$. This strategy has been frequently used to obtain the apparent energy barriers of different gases through an NATM.^[159,161,163,168,170] However, this linear fitting assumes that the energy barrier E_a is independent of temperature. This assumption is not necessarily correct because the pore diameter D_p may effectively depend on the temperature due to pore clogging by surface contaminants on the NATM surface, as discussed above.^[171,184] Considering E_a as a function of temperature T ($\partial E_a / \partial T \neq 0$), the fitted apparent energy barrier $E_a^*(i)$ can be expressed as follows

$$E_a^*(i) = \frac{\partial \left[-\frac{E_a(D_p(T), i)}{k_B T} \right]}{\partial \left(-\frac{1}{k_B T} \right)} = E_a(D_p, i) - T \frac{\partial E_a}{\partial D_p} \frac{\partial D_p}{\partial T} > E_a(D_p, i) \quad (31)$$

where $E_a(D_p, i)$ is the “real” energy barrier associated with pore translocation. Note that $\partial E_a / \partial D_p < 0$ because the energy barrier decreases as the pore size increases. Further, $\partial D_p / \partial T$ is expected to be positive because a higher temperature causes surface contaminants to desorb and alleviates pore clogging. Therefore, the apparent energy barrier $E_a^*(i)$ overestimates the “real” energy barrier $E_a(D_p, i)$. In fact, if $E_a(D_p, i)$ is small, the fitted apparent energy barrier $E_a^*(i)$ will be dominated by the $-T \frac{\partial E_a}{\partial D_p} \frac{\partial D_p}{\partial T}$ term in Equation (31), which reflects pore clogging. This may explain why the apparent energy barrier values were similar for many SLG membranes across multiple studies, although the membranes were fabricated and perforated in different ways and exhibited very different gas permeances and selectivities.^[143,159,161,163] Furthermore, this additional $-T \frac{\partial E_a}{\partial D_p} \frac{\partial D_p}{\partial T}$ term clearly depends on T , making the fitted apparent energy barrier E_a^* temperature dependent. This explains the nonlinear relation between $\ln [K(i, T)]$ and $-1/k_B T$ in some experimental results.^[62,143,159,168]

The third strategy is to use log-normal PSDs (Equation (34), Appendix). Because more unknown parameters are required in the case of log-normal PSDs, additional simplifications are needed. Based on experimental measurements, Strano and co-workers showed that the effective pore size change as a function of temperature caused by surface contamination can be expressed as $D_p = D_p^0 g(T)$, where D_p^0 is the actual pore diameter in the absence of any pore clogging induced by surface contamination, and $g(T) \in [0, 1]$ is a temperature-dependent factor which is equal to 1, if T is sufficiently high to remove all surface contaminants.^[171] Because $g(T)$ applies to all pore diameters, the temperature dependence of the PSDs of many NATMs can be represented using fewer unknown parameters, which leads to more reasonable theoretical fitting to the experimental results.^[171]

In general, the discussions above show that the temperature dependence of the PSD induced by surface contamination poses a major challenge in matching theory with experiments. Although high-temperature annealing can temporarily alleviate surface contamination on NATMs,^[161] the membrane surface would be contaminated again when it is exposed to air or to a contaminated feed gas stream. This very likely occurs in real applications. From a theoretical viewpoint, it would be helpful if the mechanism of gas transport through pores in NATMs in the presence of surface contamination could be better understood.

5. Conclusions and Outlook

Since the publication of the excellent review by Wang et al. in 2017,^[30] much progress has been made to advance gas separations using NATMs. On the theory and simulation sides, the mechanism of gas permeation through nanometer-scale pores in NATMs has been investigated in depth. Novel design ideas of NATM pores that enhance gas separation have been proposed based on simulations, including edge functionalization,^[196] asymmetrical pores,^[104,107] and continuously tunable

pore size by strain or by the overlapping of two pores.^[101,119,133] Pore nucleation and pore expansion processes have also been gaining increasing attention. On the experimental side, gas perforation methods have significantly matured. NATMs with areal pore densities exceeding 10^{16} m^{-2} (average pore distance $< 10 \text{ nm}$) have been fabricated. Further, the gas permeances and selectivities of NATMs have been greatly improved. Because of advances made in the production of functional supporting layers, the areas of NATMs have been scaled up to centimeter scale.^[164] The combination of experimental measurements and theoretical predictions have shed light on the mechanism of gas transport through confined spaces at a microscopic scale.

In spite of the great progress made as reported in our review, additional theoretical and experimental advances are required for NATMs to become practically competitive. Below, we discuss four promising and important topics that, if resolved, will facilitate the use of NATMs for gas separation.

- i) The wide and right-skewed PSD resulting from oxidative etching has become a major hurdle that constrains the gas selectivity of NATMs. Improved methods are needed to narrow down the PSD in order for NATMs to better separate some difficult yet important gas pairs like O_2/N_2 and olefin/paraffin. Theoretical investigations of the pore nucleation and pore expansion processes associated with different perforation methods would allow the research community to formulate more advanced strategies to generate narrower and more controllable PSDs. Postperforation functionalization methods, both covalent ones (ozone functionalization, fluorination) and noncovalent ones (interfacial polymerization, controlled deposition of metal, or metal oxides), could be further investigated to narrow the PSD.
- ii) Hydrocarbon adsorbates on the graphene surface (usually airborne hydrocarbon contaminants) were shown to significantly affect gas transport through graphene nanopores. However, additional investigations are needed to understand the composition of the adsorbates, the number of layers of the adsorbates and their spatial distribution with respect to the nanopore, and the mechanism of partial pore blocking at the molecular level. Methods of removing the adsorbates are of high research interest, but from an application perspective, it would be difficult to eliminate airborne hydrocarbons from the feed gas stream and the separation module. Therefore, understanding the behavior of the hydrocarbon adsorbates is important to exploit this phenomenon to our advantage. Designing specific adsorbate molecules tailored for different NATMs could open new opportunities to precisely control the PSD.
- iii) For practical applications, the areas of NATMs need to be further scaled up, while maintaining, or even improving, their quality and uniformity. This requires additional development of the functional supporting layers and the membrane fabrication process. Roll-to-roll synthesis and processing, solvent-free transfer, and interfacing with conventional polymeric supports are key technologies to enable the scale-up of NATMs. For large-scale applications, membrane packing and module design adapted for NATMs are critical. Because of the potentially high gas permeance through NATMs, creating

compact membrane systems for laboratory or medical use (e.g., to separate O₂ from other gases) may be a more realistic goal.

iv) It will be exciting to couple the selective gas permeation through NATMs with other applications, including catalytic membrane reactors,^[197] sensing,^[198] or electrochemical systems involving gases.^[199] The confined spaces created by the NATM pores may allow selective interfacial chemical reactions with controlled stereochemistry.

In summary, the development of gas selective NATMs in recent years has been inspiring. We have witnessed NATMs growing out of infancy and becoming promising next-generation gas-separation membranes. However, in spite of their tremendous potential, practically, NATMs still face significant challenges associated with gas-separation performance, robustness, and scalable production, which future theoretical, simulation, and experimental research need to address.

6. Appendix

Langmuir adsorption isotherm

$$H_{\text{surf}} = \frac{1}{p} C_{\text{surf}} = \frac{1}{p} \cdot \frac{kp}{1+kp} = \frac{k}{1+kp} \quad (32)$$

k is the equilibrium constant of adsorption.

Nonequilibrium, one-directional permeation

$$N(t) = \frac{N_0}{2} \left[1 - \exp\left(-\frac{2}{N_0} \left(\frac{dN}{dt}\right)_0 t\right) \right] \quad (33)$$

N is the number of permeated gas molecules, N_0 is the total number of gas molecules, and t is the elapsed time;^[74,93]

Log-normal pore size distribution function

$$f_{D_p}(D_p) = \frac{1}{D_p \sigma \sqrt{2\pi}} \exp\left[-\frac{(\ln D_p - \ln \mu)^2}{2\sigma^2}\right] \quad (34)$$

μ is the median pore diameter and σ is the standard deviation of $\ln D_p$.

Acknowledgements

The authors acknowledge financial support from the National Science Foundation (NSF) Grant No. CBET-1907716. This work was supported as part of the Center for Enhanced Nanofluidic Transport (CENT), an Energy Frontier Research Center funded by the U.S. Department of Energy, Office of Science, Basic Energy Sciences under Award No. DE-SC0019112. This work was also supported in part by the U.S. Army Research Laboratory (ARL) and the U.S. Army Research Office (ARO) through the Institute for Soldier Nanotechnologies (ISN), under Contract No. W911NF-13-D-0001. G.H. acknowledges the funding from Swiss National Science Foundation (Grant No. P400P2_186682).

Conflict of Interest

The authors declare no conflict of interest.

Keywords

2D materials, atomically thin membranes, gas separation, membrane separation, nanopores

Received: February 14, 2022

Revised: March 15, 2022

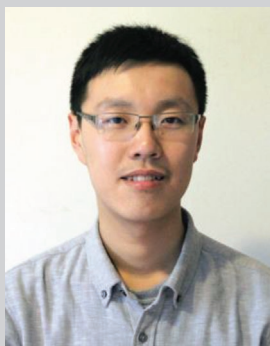
Published online: June 19, 2022

- [1] D. S. Sholl, R. P. Lively, *Nature* **2016**, 532, 435.
- [2] P. Angelini, T. Armstrong, R. Counce, W. Griffith, T. LKlasson, G. Muralidharan, C. Narula, V. Sikka, G. Closset, G. Keller, *Materials for Separation Technologies: Energy and Emission Reduction Opportunities*, DOE, EERE Office, Washington, DC, USA **2005**, p. 103.
- [3] J. L. Humphrey, G. E. Keller, *Separation Process Technology*, McGraw-Hill, Canada **1997**.
- [4] R. P. Lively, D. S. Sholl, *Nat. Mater.* **2017**, 16, 276.
- [5] R. W. Baker, *Ind. Eng. Chem. Res.* **2002**, 41, 1393.
- [6] R. W. Baker, *Membrane Technology and Applications*, John Wiley & Sons Ltd, Chichester, UK **2004**.
- [7] R. W. Baker, K. Lokhandwala, *Ind. Eng. Chem. Res.* **2008**, 47, 2109.
- [8] M. Freemantle, *Chem. Eng. News* **2005**, 83, 3.
- [9] W. J. Koros, C. Zhang, *Nat. Mater.* **2017**, 16, 289.
- [10] L. M. Robeson, *J. Membr. Sci.* **1991**, 62, 165.
- [11] L. M. Robeson, *J. Membr. Sci.* **2008**, 320, 390.
- [12] B. D. Freeman, *Macromolecules* **1999**, 32, 375.
- [13] J. Van den Bergh, W. Zhu, J. Gascon, J. Moulijn, F. Kapteijn, *J. Membr. Sci.* **2008**, 316, 35.
- [14] S. Himeno, T. Tomita, K. Suzuki, K. Nakayama, K. Yajima, S. Yoshida, *Ind. Eng. Chem. Res.* **2007**, 46, 6989.
- [15] Z. Xie, T. Li, N. L. Rosi, M. A. Carreon, *J. Mater. Chem. A* **2014**, 2, 1239.
- [16] J. A. Bohrman, M. A. Carreon, *Chem. Commun.* **2012**, 48, 5130.
- [17] R. M. de Vos, H. Verweij, *Science* **1998**, 279, 1710.
- [18] C. W. Jones, W. J. Koros, *Carbon* **1994**, 32, 1419.
- [19] H. Richter, H. Voss, N. Kaltenborn, S. Kämnitz, A. Wollbrink, A. Feldhoff, J. Caro, S. Roitsch, I. Voigt, *Angew. Chem., Int. Ed.* **2017**, 56, 7760.
- [20] X. Ma, R. Swaidan, B. Teng, H. Tan, O. Salinas, E. Litwiller, Y. Han, I. Pinnau, *Carbon* **2013**, 62, 88.
- [21] S. Husain, W. J. Koros, *J. Membr. Sci.* **2007**, 288, 195.
- [22] T.-S. Chung, L. Y. Jiang, Y. Li, S. Kulprathipanja, *Prog. Polym. Sci.* **2007**, 32, 483.
- [23] A. K. Geim, *Science* **2009**, 324, 1530.
- [24] L. Huang, M. Zhang, C. Li, G. Shi, *J. Phys. Chem. Lett.* **2015**, 6, 2806.
- [25] S. Lin, C.-J. Shih, V. Sresht, A. Govind Rajan, M. S. Strano, D. Blankschtein, *Adv. Colloid Interface Sci.* **2017**, 244, 36.
- [26] Y. Shi, C. Hamsen, X. Jia, K. K. Kim, A. Reina, M. Hofmann, A. L. Hsu, K. Zhang, H. Li, Z.-Y. Juang, Mildred. S. Dresselhaus, L.-J. Li, J. Kong, *Nano Lett.* **2010**, 10, 4134.
- [27] S. Manzeli, D. Ovchinnikov, D. Pasquier, O. V. Yazyev, A. Kis, *Nat. Rev. Mater.* **2017**, 2, 17033.
- [28] B. M. Yoo, J. E. Shin, H. D. Lee, H. B. Park, *Curr. Opin. Chem. Eng.* **2017**, 16, 39.
- [29] D. Jiang, V. R. Cooper, S. Dai, *Nano Lett.* **2009**, 9, 4019.
- [30] L. Wang, M. S. H. Boutillier, P. R. Kidambi, D. Jang, N. G. Hadjiconstantinou, R. Karnik, *Nat. Nanotechnol.* **2017**, 12, 509.
- [31] F. Moghadam, H. B. Park, *Curr. Opin. Chem. Eng.* **2018**, 20, 28.
- [32] I. Frank, D. M. Tanenbaum, A. Van der Zande, P. L. McEuen, *J. Vac. Sci. Technol. B* **2007**, 25, 2558.

- [33] J. Feng, M. Graf, K. Liu, D. Ovchinnikov, D. Dumcenco, M. Heiranian, V. Nandigana, N. R. Aluru, A. Kis, A. Radenovic, *Nature* **2016**, 536, 197.
- [34] J. S. Bunch, S. S. Verbridge, J. S. Alden, A. M. van der Zande, J. M. Parpia, H. G. Craighead, P. L. McEuen, *Nano Lett.* **2008**, 8, 2458.
- [35] V. Berry, *Carbon* **2013**, 62, 1.
- [36] P. Z. Sun, Q. Yang, W. J. Kuang, Y. V. Stebunov, W. Q. Xiong, J. Yu, R. R. Nair, M. I. Katsnelson, S. J. Yuan, I. V. Grigorieva, M. Lozada-Hidalgo, F. C. Wang, A. K. Geim, *Nature* **2020**, 579, 229.
- [37] J. Wijmans, R. Baker, *J. Membr. Sci.* **1995**, 107, 1.
- [38] A. Turchanin, A. Götzhäuser, *Adv. Mater.* **2016**, 28, 6075.
- [39] L. Cheng, G. Liu, J. Zhao, W. Jin, *Acc. Mater. Res.* **2021**, 2, 114.
- [40] M. Liu, P. Andrew Gurr, Q. Fu, P. Webley, G. G. Qiao, *J. Mater. Chem. A* **2018**, 6, 23169.
- [41] B. Mi, *Science* **2019**, 364, 1033.
- [42] G. Liu, W. Jin, N. Xu, *Chem. Soc. Rev.* **2015**, 44, 5016.
- [43] H. W. Yoon, Y. H. Cho, H. B. Park, *Philos. Trans. R. Soc. Math. Phys. Eng. Sci.* **2016**, 374, 20150024.
- [44] A. G. Rajan, K. S. Sillmore, J. Swett, A. W. Robertson, J. H. Warner, D. Blankschtein, M. S. Strano, *Nat. Mater.* **2019**, 18, 129.
- [45] T. Pham, A. L. Gibb, Z. Li, S. M. Gilbert, C. Song, S. G. Louie, A. Zettl, *Nano Lett.* **2016**, 16, 7142.
- [46] J. C. Meyer, A. Chuvilin, G. Algara-Siller, J. Biskupek, U. Kaiser, *Nano Lett.* **2009**, 9, 2683.
- [47] S. M. Gilbert, G. Dunn, A. Azizi, T. Pham, B. Shevitski, E. Dimitrov, S. Liu, S. Aloni, A. Zettl, *Sci. Rep.* **2017**, 7, 15096.
- [48] G. Hee Ryu, H. Ju Park, J. Ryou, J. Park, J. Lee, G. Kim, H. Suk Shin, C. W. Bielawski, R. S. Ruoff, S. Hong, Z. Lee, *Nanoscale* **2015**, 7, 10600.
- [49] J. Kotakoski, C. H. Jin, O. Lehtinen, K. Suenaga, A. V. Krashenninnikov, *Phys. Rev. B* **2010**, 82, 113404.
- [50] Y. Shen, T. Xu, X. Tan, L. He, K. Yin, N. Wan, L. Sun, *Adv. Mater.* **2018**, 30, 1705954.
- [51] J.-A. Ke, S. Garaj, S. Gradečak, *ACS Appl. Mater. Interfaces* **2019**, 11, 26228.
- [52] S. Jennings, *J. Aerosol Sci.* **1988**, 19, 159.
- [53] R. A. Sampson, *Philos. Trans. R. Soc., A* **1891**, 182, 449.
- [54] K.-K. Tio, S. S. Sadhal, *Appl. Sci. Res.* **1994**, 52, 1.
- [55] K. H. Jensen, A. X. Valente, H. A. Stone, *Phys. Fluids* **2014**, 26, 052004.
- [56] A. F. Ismail, K. Khulbe, T. Matsuura, *Gas Separation Membranes: Polymeric and Inorganic*, Springer International Publishing, Cham, Switzerland **2015**.
- [57] P. Atkins, J. De Paula, *Atkins' Physical Chemistry*, 8th ed., Oxford University Press, New York **2006**.
- [58] K. J. Laidler, J. H. Meiser, *Physical Chemistry*, Benjamin/Cummings Pub. Co, Menlo Park, CA, USA **1982**.
- [59] Z. Yuan, A. Govind Rajan, R. P. Misra, L. W. Drahushuk, K. V. Agrawal, M. S. Strano, D. Blankschtein, *ACS Nano* **2017**, 11, 7974.
- [60] L. Wang, L. W. Drahushuk, L. Cantley, S. P. Koenig, X. Liu, J. Pellegrino, M. S. Strano, J. S. Bunch, *Nat. Nanotechnol.* **2015**, 10, 785.
- [61] C. Sun, M. S. H. Boutilier, H. Au, P. Poesio, B. Bai, R. Karnik, N. G. Hadjiconstantinou, *Langmuir* **2014**, 30, 675.
- [62] Z. Yuan, J. D. Benck, Y. Eatmon, D. Blankschtein, M. S. Strano, *Nano Lett.* **2018**, 18, 5057.
- [63] Z. Yuan, R. P. Misra, A. G. Rajan, M. S. Strano, D. Blankschtein, *ACS Nano* **2019**, 13, 11809.
- [64] H. Du, J. Li, J. Zhang, G. Su, X. Li, Y. Zhao, *J. Phys. Chem. C* **2011**, 115, 23261.
- [65] L. W. Drahushuk, M. S. Strano, *Langmuir* **2012**, 28, 16671.
- [66] C. Sun, B. Bai, *Chem. Eng. Sci.* **2017**, 165, 186.
- [67] K. Solvik, J. A. Weaver, A. M. Brockway, J. Schrier, *J. Phys. Chem. C* **2013**, 117, 17050.
- [68] K. S. W. Sing, *Pure Appl. Chem.* **1985**, 57, 603.
- [69] S. Brunauer, P. H. Emmett, E. Teller, *J. Am. Chem. Soc.* **1938**, 60, 309.
- [70] S. Blankenburg, M. Bieri, R. Fasel, K. Müllen, C. A. Pignedoli, D. Passerone, *Small* **2010**, 6, 2266.
- [71] R. Lu, Z. Meng, D. Rao, Y. Wang, Q. Shi, Y. Zhang, E. Kan, C. Xiao, K. Deng, *Nanoscale* **2014**, 6, 9960.
- [72] A. W. Hauser, P. Schwerdtfeger, *Phys. Chem. Chem. Phys.* **2012**, 14, 13292.
- [73] H. Liu, S. Dai, D. Jiang, *Nanoscale* **2013**, 5, 9984.
- [74] C. Sun, B. Bai, *Sci. Bull.* **2017**, 62, 554.
- [75] H. Liu, Z. Chen, S. Dai, D. Jiang, *J. Solid State Chem.* **2015**, 224, 2.
- [76] D. Chandler, *J. Chem. Phys.* **1978**, 68, 2959.
- [77] S. M. Auerbach, *Int. Rev. Phys. Chem.* **2000**, 19, 155.
- [78] J. Azamat, A. Khataee, S. W. Joo, *J. Mol. Model.* **2016**, 22, 82.
- [79] D. Frenkel, B. Smit, in *Understanding Molecular Simulations*, 2nd ed. (Eds: D. Frenkel, B. Smit), Academic Press, San Diego, CA, USA **2002**, p. 431.
- [80] D. Frenkel, B. Smit, *Understanding Molecular Simulations*, 2nd ed., Academic Press, San Diego, CA, USA **2002**, p. 63.
- [81] M. Hankel, Y. Jiao, A. Du, S. K. Gray, S. C. Smith, *J. Phys. Chem. C* **2012**, 116, 6672.
- [82] A. W. Hauser, J. Schrier, P. Schwerdtfeger, *J. Phys. Chem. C* **2012**, 116, 10819.
- [83] M. Lalitha, S. Lakshmipathi, S. K. Bhatia, *J. Phys. Chem. C* **2015**, 119, 20940.
- [84] M. S. Motalebipour, J. Karimi-Sabet, A. Maghari, *Phys. Chem. Chem. Phys.* **2019**, 21, 12414.
- [85] J. Schrier, J. McClain, *Chem. Phys. Lett.* **2012**, 521, 118.
- [86] H. Au, *Ph.D. Thesis*, Massachusetts Institute of Technology, Cambridge, MA, USA **2012**.
- [87] S. W. Cranford, M. J. Buehler, *Nanoscale* **2012**, 4, 4587.
- [88] G. Lei, C. Liu, H. Xie, F. Song, *Chem. Phys. Lett.* **2014**, 599, 127.
- [89] H. Liu, S. Dai, D. Jiang, *Solid State Commun.* **2013**, 101, 175.
- [90] J. Schrier, *ACS Appl. Mater. Interfaces* **2012**, 4, 3745.
- [91] M. Shan, Q. Xue, N. Jing, C. Ling, T. Zhang, Z. Yan, J. Zheng, *Nanoscale* **2012**, 4, 5477.
- [92] C. Sun, B. Wen, B. Bai, *Chem. Eng. Sci.* **2015**, 138, 616.
- [93] B. Wen, C. Sun, B. Bai, *Phys. Chem. Chem. Phys.* **2015**, 17, 23619.
- [94] T. Wu, Q. Xue, C. Ling, M. Shan, Z. Liu, Y. Tao, X. Li, *J. Phys. Chem. C* **2014**, 118, 7369.
- [95] J. Azamat, A. Khataee, F. Sadikoglu, *RSC Adv.* **2016**, 6, 94911.
- [96] Y. Wang, Q. Yang, J. Li, J. Yang, C. Zhong, *Phys. Chem. Chem. Phys.* **2016**, 18, 8352.
- [97] S. Esfandiarpour, M. Fazli, M. D. Ganji, *Sci. Rep.* **2017**, 7, 16561.
- [98] A. Khakpay, F. Rahmani, S. Nouranian, P. Scovazzo, *J. Phys. Chem. C* **2017**, 121, 12308.
- [99] C. Sun, B. Bai, *J. Phys. Chem. C* **2018**, 122, 6178.
- [100] G. Tronci, F. Raffone, G. Cicero, G. Tronci, F. Raffone, G. Cicero, *Appl. Sci.* **2018**, 8, 1547.
- [101] S. Wang, S. Dai, D. Jiang, *ACS Appl. Nano Mater.* **2019**, 2, 379.
- [102] S. Wang, Z. Tian, S. Dai, D. Jiang, *Nanoscale* **2018**, 10, 14660.
- [103] S. Wang, S. Dai, D. Jiang, *Phys. Chem. Chem. Phys.* **2019**, 21, 16310.
- [104] M. Liu, D. Song, X. Wang, C. Sun, D. Jing, *J. Phys. Chem. Lett.* **2020**, 11, 6359.
- [105] Y. Xu, H. Zhu, M. Wang, J. Xu, C. Yang, *Ind. Eng. Chem. Res.* **2020**, 59, 9215.
- [106] C. Sun, K. Luo, R. Zhou, B. Bai, *Phys. Chem. Chem. Phys.* **2021**, 23, 7057.
- [107] C. Sun, R. Zhou, B. Bai, Y. Lin, B. Li, *J. Phys. Chem. C* **2021**, 125, 3047.
- [108] X. Qin, Q. Meng, Y. Feng, Y. Gao, *Surf. Sci.* **2013**, 607, 153.
- [109] A. Ambrosetti, P. L. Silvestrelli, *J. Phys. Chem. C* **2014**, 118, 19172.

- [110] W. Hu, X. Wu, Z. Li, J. Yang, *Phys. Chem. Chem. Phys.* **2013**, *15*, 5753.
- [111] Y. Jiao, A. Du, M. Hankel, Z. Zhu, V. Rudolph, S. C. Smith, *Chem. Commun.* **2011**, 47, 11843.
- [112] Y. Li, Z. Zhou, P. Shen, Z. Chen, *Chem. Commun.* **2010**, 46, 3672.
- [113] R. Lu, D. Rao, Z. Lu, J. Qian, F. Li, H. Wu, Y. Wang, C. Xiao, K. Deng, E. Kan, W. Deng, *J. Phys. Chem. C* **2012**, *116*, 21291.
- [114] J. Schrier, *J. Phys. Chem. Lett.* **2010**, *1*, 2284.
- [115] H. Zhang, X. He, M. Zhao, M. Zhang, L. Zhao, X. Feng, Y. Luo, *J. Phys. Chem. C* **2012**, *116*, 16634.
- [116] Y. Zhang, F. Hao, H. Xiao, C. Liu, X. Shi, X. Chen, *Int. J. Hydrog. Energy* **2016**, *41*, 23067.
- [117] A. Bian, Y. Dai, J. Yang, *Nanoscale* **2017**, *9*, 17505.
- [118] K. Yin, S. Huang, X. Chen, X. Wang, J. Kong, Y. Chen, J. Xue, *ACS Appl. Mater. Interfaces* **2018**, *10*, 28909.
- [119] E. Gao, C. Zhang, K. Zhou, N. Wei, *ACS Appl. Nano Mater.* **2020**, *3*, 11474.
- [120] Y. Li, L. Zhang, C. Wu, *Appl. Surf. Sci.* **2020**, 525, 146524.
- [121] S. Wei, S. Zhou, Z. Wu, M. Wang, Z. Wang, W. Guo, X. Lu, *Appl. Surf. Sci.* **2018**, 441, 631.
- [122] C. Huang, H. Wu, K. Deng, W. Tang, E. Kan, *Phys. Chem. Chem. Phys.* **2014**, *16*, 25755.
- [123] A. M. Brockway, J. Schrier, *J. Phys. Chem. C* **2013**, *117*, 393.
- [124] Y. Tao, Q. Xue, Z. Liu, M. Shan, C. Ling, T. Wu, X. Li, *ACS Appl. Mater. Interfaces* **2014**, *6*, 8048.
- [125] Y. Zhang, Q. Shi, Y. Liu, Y. Wang, Z. Meng, C. Xiao, K. Deng, D. Rao, R. Lu, *J. Phys. Chem. C* **2015**, *119*, 19826.
- [126] Y. Qu, F. Li, M. Zhao, *J. Phys. Chem. C* **2017**, *121*, 17925.
- [127] Y. Zhang, Z. Meng, Q. Shi, H. Gao, Y. Liu, Y. Wang, D. Rao, K. Deng, R. Lu, *J. Phys. Chem. Matter* **2017**, *29*, 375201.
- [128] L. Zhao, P. Sang, S. Guo, X. Liu, J. Li, H. Zhu, W. Guo, *Appl. Surf. Sci.* **2017**, 405, 455.
- [129] Y.-C. Rao, Z.-Q. Chu, X. Gu, X.-M. Duan, *Comput. Mater. Sci.* **2019**, *161*, 53.
- [130] L. Zhu, Q. Xue, X. Li, T. Wu, Y. Jin, W. Xing, *J. Mater. Chem. A* **2015**, *3*, 21351.
- [131] F. Vallejos-Burgos, F.-X. Coudert, K. Kaneko, *Nat. Commun.* **2018**, *9*, 1812.
- [132] Y. Wang, W. Wang, S. Zhu, L. Guo, Z. Zhang, P. Li, *Comput. Mater. Sci.* **2018**, 143, 277.
- [133] M. Wang, Z. Wang, S. Zhou, J. Wang, S. Liu, S. Wei, W. Guo, X. Lu, *Appl. Surf. Sci.* **2020**, 506, 144675.
- [134] S. Jalil Mahdizadeh, E. K. Goharshadi, *RSC Adv.* **2020**, *10*, 24255.
- [135] S. Lin, M. Xu, Z. Qu, Y. Liang, Y. Li, W. Cui, J. Shi, Q. Zeng, J. Hao, Y. Li, *Phys. Chem. Chem. Phys.* **2020**, *22*, 22778.
- [136] Y. Wang, Q. Yang, C. Zhong, J. Li, *Appl. Surf. Sci.* **2017**, 407, 532.
- [137] Z. Tian, S. Dai, D. Jiang, *ACS Appl. Mater. Interfaces* **2015**, *7*, 13073.
- [138] S. P. Koenig, L. Wang, J. Pellegrino, J. S. Bunch, *Nat. Nanotechnol.* **2012**, *7*, 728.
- [139] D. Marx, P. Nielaba, *Phys. Rev. A* **1992**, *45*, 8968.
- [140] G. M. Torrie, J. P. Valleau, *J. Comput. Phys.* **1977**, *23*, 187.
- [141] K. Nieszporek, M. Drach, *Phys. Chem. Chem. Phys.* **2014**, *17*, 1018.
- [142] S. C. O'Hern, M. S. H. Boutilier, J.-C. Idrobo, Y. Song, J. Kong, T. Laoui, M. Atieh, R. Karnik, *Nano Lett.* **2014**, *14*, 1234.
- [143] G. He, S. Huang, L. F. Villalobos, M. T. Vahdat, M. D. Guiver, J. Zhao, W.-C. Lee, M. Mensi, K. V. Agrawal, *Adv. Funct. Mater.* **2020**, *30*, 2003979.
- [144] K. S. Novoselov, A. K. Geim, S. V. Morozov, D. Jiang, Y. Zhang, S. V. Dubonos, I. V. Grigorieva, A. A. Firsov, *Science* **2004**, 306, 666.
- [145] X. Li, W. Cai, J. An, S. Kim, J. Nah, D. Yang, R. Piner, A. Velamakanni, I. Jung, E. Tutuc, S. K. Banerjee, L. Colombo, R. S. Ruoff, *Science* **2009**, 324, 1312.
- [146] F. Banhart, J. Kotakoski, A. V. Krasheninnikov, *ACS Nano* **2011**, *5*, 26.
- [147] A. T. Kuan, B. Lu, P. Xie, T. Szalay, J. A. Golovchenko, *Appl. Phys. Lett.* **2015**, *106*, 203109.
- [148] C. J. Russo, J. A. Golovchenko, *Proc. Natl. Acad. Sci. USA* **2012**, *109*, 5953.
- [149] K. Choi, A. Droudian, R. M. Wyss, K.-P. Schlichting, H. G. Park, *Sci. Adv.* **2018**, *4*, eaau0476.
- [150] K. Celebi, J. Buchheim, R. M. Wyss, A. Droudian, P. Gasser, I. Shorubalko, J.-I. Kye, C. Lee, H. G. Park, *Science* **2014**, 344, 289.
- [151] I. E. Rostor, R. J. Dolleman, H. Licon, M. Lee, M. Šiškins, H. Lebius, L. Madau, M. Schleberger, F. Aljani, H. S. J. van der Zant, P. G. Steeneken, *Nat. Commun.* **2020**, *11*, 6025.
- [152] M. S. H. Boutilier, N. G. Hadjiconstantinou, R. Karnik, *Nanotechnology* **2017**, *28*, 184003.
- [153] J. P. Thiruraman, S. A. Dar, P. M. Das, N. Hassani, M. Neek-Amal, A. Keerthi, M. Drndić, B. Radha, *Sci. Adv.* **2020**, *6*, eabc7927.
- [154] J. Liu, L. Jin, F. I. Allen, Y. Gao, P. Ci, F. Kang, J. Wu, *Nano Lett.* **2021**, *21*, 2183.
- [155] A. V. Krasheninnikov, F. Banhart, *Nat. Mater.* **2007**, *6*, 723.
- [156] M. S. H. Boutilier, D. Jang, J.-C. Idrobo, P. R. Kidambi, N. G. Hadjiconstantinou, R. Karnik, *ACS Nano* **2017**, *11*, 5726.
- [157] K.-P. Schlichting, D. Poulikakos, *ACS Appl. Mater. Interfaces* **2020**, *12*, 36468.
- [158] W. Guo, S. M. Mahurin, R. R. Unocic, H. Luo, S. Dai, *Nano Lett.* **2020**, *20*, 7995.
- [159] S. Huang, M. Dakhchoune, W. Luo, E. Oveisi, G. He, M. Rezaei, J. Zhao, D. T. L. Alexander, A. Züttel, M. S. Strano, K. V. Agrawal, *Nat. Commun.* **2018**, *9*, 2632.
- [160] G. He, S. Huang, L. F. Villalobos, J. Zhao, M. Mensi, E. Oveisi, M. Rezaei, K. V. Agrawal, *Energy Environ. Sci.* **2019**, *12*, 3305.
- [161] J. Zhao, G. He, S. Huang, L. F. Villalobos, M. Dakhchoune, H. Bassas, K. V. Agrawal, *Sci. Adv.* **2019**, *5*, eaav1851.
- [162] D. Hou, S. Zhang, X. Chen, R. Song, D. Zhang, A. Yao, J. Sun, W. Wang, L. Sun, B. Chen, Z. Liu, L. Wang, *ACS Appl. Mater. Interfaces* **2021**, *13*, 10328.
- [163] S. Huang, S. Li, L. F. Villalobos, M. Dakhchoune, M. Micari, D. J. Babu, M. T. Vahdat, M. Mensi, E. Oveisi, K. V. Agrawal, *Sci. Adv.* **2021**, *7*, eabf0116.
- [164] W.-C. Lee, L. Bondaz, S. Huang, G. He, M. Dakhchoune, K. V. Agrawal, *J. Membr. Sci.* **2021**, 618, 118745.
- [165] K.-J. Hsu, L. F. Villalobos, S. Huang, H.-Y. Chi, M. Dakhchoune, W.-C. Lee, G. He, M. Mensi, K. V. Agrawal, *ACS Nano* **2021**, *15*, 13230.
- [166] S. Huang, S. Li, K.-J. Hsu, L. F. Villalobos, K. V. Agrawal, *J. Membr. Sci.* **2021**, 637, 119628.
- [167] M. S. H. Boutilier, C. Sun, S. C. O'Hern, H. Au, N. G. Hadjiconstantinou, R. Karnik, *ACS Nano* **2014**, *8*, 841.
- [168] M. H. Khan, M. Moradi, M. Dakhchoune, M. Rezaei, S. Huang, J. Zhao, K. V. Agrawal, *Carbon* **2019**, 153, 458.
- [169] S. Nikkho, M. Mirzaei, J. Karimi Sabet, M. A. Moosavian, S. M. Hedayat, *Sep. Purif. Technol.* **2020**, 232, 115972.
- [170] M. Rezaei, S. Li, S. Huang, K. V. Agrawal, *J. Membr. Sci.* **2020**, 612, 118406.
- [171] Z. Yuan, G. He, S. Faucher, M. Kuehne, S. X. Li, D. Blankschtein, M. S. Strano, *Adv. Mater.* **2021**, *33*, 2104308.
- [172] S. C. O'Hern, D. Jang, S. Bose, J.-C. Idrobo, Y. Song, T. Laoui, J. Kong, R. Karnik, *Nano Lett.* **2015**, *15*, 3254.
- [173] S. P. Surwade, S. N. Smirnov, I. V. Vlasiouk, R. R. Unocic, G. M. Veith, S. Dai, S. M. Mahurin, *Nat. Nanotechnol.* **2015**, *10*, 459.
- [174] H.-T. Chin, J.-J. Lee, M. Hofmann, Y.-P. Hsieh, *Sci. Rep.* **2018**, *8*, 4046.
- [175] K. Balasubramanian, T. Biswas, P. Ghosh, S. Suran, A. Mishra, R. Mishra, R. Sachan, M. Jain, M. Varma, R. Pratap, S. Raghavan, *Nat. Commun.* **2019**, *10*, 1090.
- [176] S. Choubak, M. Biron, P. L. Levesque, R. Martel, P. Desjardins, *J. Phys. Chem. Lett.* **2013**, *4*, 1100.

- [177] P. R. Kidambi, G. D. Nguyen, S. Zhang, Q. Chen, J. Kong, J. Warner, A.-P. Li, R. Karnik, *Adv. Mater.* **2018**, *30*, 1804977.
- [178] P. R. Kidambi, C. Ducati, B. Dlubak, D. Gardiner, R. S. Weatherup, M.-B. Martin, P. Seneor, H. Coles, S. Hofmann, *J. Phys. Chem. C* **2012**, *116*, 22492.
- [179] L. Wang, X. Zhang, H. L. W. Chan, F. Yan, F. Ding, *J. Am. Chem. Soc.* **2013**, *135*, 4476.
- [180] J. Bai, X. Zhong, S. Jiang, Y. Huang, X. Duan, *Nat. Nanotechnol.* **2010**, *5*, 190.
- [181] M. Bieri, M. Treier, J. Cai, K. Ait-Mansour, P. Ruffieux, O. Gröning, P. Gröning, M. Kastler, R. Rieger, X. Feng, K. Müllen, R. Fasel, *Chem. Commun.* **2009**, 6919.
- [182] D. J. Murray, D. D. Patterson, P. Payamyar, R. Bhola, W. Song, M. Lackinger, A. D. Schlüter, B. T. King, *J. Am. Chem. Soc.* **2015**, *137*, 3450.
- [183] G. Li, Y. Li, H. Liu, Y. Guo, Y. Li, D. Zhu, *Chem. Commun.* **2010**, 46, 3256.
- [184] Z. Yuan, A. Govind Rajan, G. He, R. P. Misra, M. S. Strano, D. Blankschtein, *ACS Nano* **2021**, *15*, 1727.
- [185] S. W. Smith, *Scientist and Engineer's Guide to Digital Signal Processing*, California Technical Pub, San Diego, CA, USA **1997**.
- [186] D. C. Montgomery, G. C. Runger, *Applied Statistics and Probability for Engineers*, John Wiley And Sons, New York **2014**.
- [187] P. R. Kidambi, D. Jang, J.-C. Idrobo, M. S. H. Boutilier, L. Wang, J. Kong, R. Karnik, *Adv. Mater.* **2017**, *29*, 1700277.
- [188] P. Cheng, M. M. Kelly, N. K. Moehring, W. Ko, A.-P. Li, J. C. Idrobo, M. S. H. Boutilier, P. R. Kidambi, *Nano Lett.* **2020**, *20*, 5951.
- [189] J.-Y. Hong, Y. C. Shin, A. Zubair, Y. Mao, T. Palacios, M. S. Dresselhaus, S. H. Kim, J. Kong, *Adv. Mater.* **2016**, *28*, 2382.
- [190] H. H. Kim, S. K. Lee, S. G. Lee, E. Lee, K. Cho, *Adv. Funct. Mater.* **2016**, *26*, 2070.
- [191] L. Wang, C. M. Williams, M. S. H. Boutilier, P. R. Kidambi, R. Karnik, *Nano Lett.* **2017**, *17*, 3081.
- [192] A. T. Rodriguez, X. Li, J. Wang, W. A. Steen, H. Fan, *Adv. Funct. Mater.* **2007**, *17*, 2710.
- [193] Y. Yang, X. Yang, L. Liang, Y. Gao, H. Cheng, X. Li, M. Zou, R. Ma, Q. Yuan, X. Duan, *Science* **2019**, *364*, 1057.
- [194] B. Song, G. F. Schneider, Q. Xu, G. Pandraud, C. Dekker, H. Zandbergen, *Nano Lett.* **2011**, *11*, 2247.
- [195] L. F. Villalobos, S. Huang, M. Dakhchoune, G. He, W.-C. Lee, K. V. Agrawal, *Carbon* **2021**, *173*, 980.
- [196] Y. Li, Y. Linghu, C. Wu, *ACS Appl. Mater. Interfaces* **2020**, *12*, 20096.
- [197] J. G. Sanchez Marcano, T. T. Tsotsis, *Catalytic Membranes and Membrane Reactors*, Wiley-VCH, Weinheim, Germany **2002**.
- [198] B. Sun, R. N. McCay, S. Goswami, Y. Xu, C. Zhang, Y. Ling, J. Lin, Z. Yan, *Adv. Mater.* **2018**, *30*, 1804327.
- [199] W.-J. Kwak, Rosy, D. Sharon, C. Xia, H. Kim, L. R. Johnson, P. G. Bruce, L. F. Nazar, Y.-K. Sun, A. A. Frimer, M. Noked, S. A. Freunberger, D. Aurbach, *Chem. Rev.* **2020**, *120*, 6626.



Zhe Yuan received his B.E. degree in chemical engineering from Tsinghua University, and his Ph.D. in chemical engineering from Massachusetts Institute of Technology (MIT) under the supervision of Prof. Daniel Blankschtein and Prof. Michael S. Strano. He is currently a postdoctoral associate working with Prof. James M. Tour at Rice University. His research focuses on separation processes facilitated by porous 2D materials and amorphous carbon-based materials.



Guangwei He is an associate professor at the School of Chemical Engineering and Technology, Tianjin University. He received his Ph.D. from Tianjin University under the supervision of Prof. Zhongyi Jiang in 2016. Since then, he joined Prof. Kumar Varoon Agrawal's group at EPFL as a postdoctoral researcher. In 2019, he joined Prof. Michael S. Strano's group at MIT as a postdoctoral researcher. His research interests include molecular-sieving membranes made of single-atom-thick film, MOFs, and COFs.



Rahul Prasanna Misra received his B.Tech in chemical engineering from the Indian Institute of Technology, Kharagpur, India, and his Master of Science in Chemical Engineering Practice (MSCEP) and Ph.D. in chemical engineering from the Massachusetts Institute of Technology. As part of his Ph.D. under the supervision of Prof. Daniel Blankschtein, he developed a multiscale framework to self-consistently model electronic polarization effects in interfacial thermodynamics and nanoscale transport phenomena. Currently, he is a postdoctoral associate working with Prof. Daniel Blankschtein, where his research focuses on atomistic modeling of pure water and electrolytes in nanofluidic applications.



Michael S. Strano is the Carbon P. Dubbs Professor of Chemical Engineering at the Massachusetts Institute of Technology (MIT). He received his Ph.D. from the University of Delaware in Chemical Engineering. He was a postdoctoral research fellow at Rice University under the guidance of Nobel Laureate Richard E. Smalley. His research focuses on biomolecule/nanoparticle interactions and the surface chemistry of low-dimensional systems, nanoelectronics, nanoparticle separations, and applications of vibrational spectroscopy to nanotechnology.



Daniel Blankschtein is the Herman P. Meissner (1929) Professor of Chemical Engineering at the Massachusetts Institute of Technology (MIT). He received his B.Sc. (1977), M.Sc. (1979), and Ph.D. (1983) in physics from Tel-Aviv University. He joined MIT as a Weizmann postdoctoral research fellow in 1982, and then worked in the Department of Physics and Center for Materials Science and Engineering as a Bantrell postdoctoral research fellow from 1984 to 1986. He joined MIT's department of Chemical Engineering in 1986. His research focuses on surfactant self-assembly, surface phenomena, colloid science, biological separations, transdermal drug delivery, 2D nanomaterials, and gas separations.